# Marginated aberrant red blood cells induce pathologic vascular stress fluctuations in a computational model of hematologic disorders

Xiaopo Cheng,<sup>1</sup> Christina Caruso,<sup>2</sup> Wilbur A. Lam,<sup>2,3\*</sup> Michael D. Graham<sup>1\*</sup>

<sup>1</sup>Department of Chemical and Biological Engineering, University of Wisconsin-Madison, Madison, WI 53706, USA

<sup>2</sup>Aflac Cancer and Blood Disorders Center of Children's Healthcare of Atlanta,
 Department of Pediatrics, Emory University School of Medicine, Atlanta, GA 30307, USA
 <sup>3</sup>Wallace H. Coulter Department of Biomedical Engineering,
 Georgia Institute of Technology and Emory University, Atlanta, GA 30332, USA

\*To whom correspondence should be addressed; E-mail: wilbur.lam@emory.edu, mdgraham@wisc.edu

Red blood cell (RBC) disorders such as sickle cell disease affect billions world-wide. While much attention focuses on altered properties of aberrant RBCs and corresponding hemodynamic changes, RBC disorders are also associated with vascular dysfunction, whose origin remains unclear, and which provoke severe consequences including stroke. Little research has explored whether biophysical alterations of RBCs affect vascular function. Here we employ a detailed computational model of blood that enables characterization of cell distributions and vascular stresses in blood disorders, and compare simulation results with experimental observations. Aberrant RBCs, with their smaller size and higher stiffness, concentrate near vessel walls (marginate) due to con-

trasts in physical properties relative to normal cells. In a curved channel exemplifying the geometric complexity of the microcirculation, these cells distribute heterogeneously, indicating the importance of geometry. Marginated cells generate large transient stress fluctuations on vessel walls, indicating a mechanism for the observed vascular inflammation.

**Short title** Marginated aberrant RBCs cause vascular stress

**Teaser** In blood disorders, aberrant red blood cells drive stress fluctuations at blood vessel walls leading to endothelial inflammation.

# Introduction

Disorders that affect red blood cells (RBCs) encompass a diverse range of conditions with substantial implications for human health, highlighting the need to comprehend their underlying mechanisms and effects. One prominent example is sickle cell disease, a monogenic hemoglobin disorder resulting in stiffened and sickle-shaped or otherwise deformed RBCs. Sickle cell disease leads to chronic pain, organ damage, and life-threatening complications (1). In addition, the recent global pandemic of COVID-19, caused by SARS-CoV-2 infection can lead to substantial alterations of RBCs (2). Emerging evidence suggests that organ dysfunction associated with severe COVID-19 may result from endothelial damage and microvascular thrombosis (3). Sepsis, a life-threatening condition arising from severe systemic infection, disrupts the morphology and function of RBCs, precipitating organ failure, hypotension, and increased mortality rates (4). Iron deficiency anemia, adversely affects RBC production and their oxygen-carrying capacity, consequently exerting detrimental effects on the cardiovascular system (5). Hereditary spherocytosis, which is characterized by abnormal spherical-shaped RBC,

affects cell membrane stability and increases susceptibility to hemolysis (6). A comprehensive exploration of these RBC disorders will enable a deeper understanding of their intricacies and the crucial significance of maintaining RBC health and functionality and alleviating vasculopathy.

In individuals with blood disorders, endothelial cells lining the blood vessels are often dysfunctional and in a pro-inflammatory state, increasing the risk of stroke and atherosclerosis (7–11). In particular, stroke, a predominant cause of mortality in sickle cell disease (SCD), often occurs in highly tortuous cerebral arteries and is associated with endothelial inflammation and chronic vasculopathy. In patients with cardiovascular disease and iron deficiency anemia (IDA), improved disease outcomes were observed with iron supplementation and subsequent resolution of IDA. (12); however, the underlying pathophysiologic basis for the association remains unknown. The interplay among adhesive RBC-endothelial interactions, inflammatory cytokines, and hemolysis all contribute to vasculopathy in blood disorders, however the potential contribution of the altered physical properties of aberrant RBCs, particularly shape and stiffness, to the hemodynamic environment experienced by the vascular endothelium remains poorly understood. This topic is the focus of the present work.

Vascular geometries contribute to vasculopathy in blood disorders (13). The vascular system is comprised of diverse geometries, including normal complexities such as curves and bifurcations as well as pathologic ones such as aneurysms and stenoses, and variations in vascular geometry cause substantial changes in the local shear stress profile during blood flow, which are known to induce endothelial proinflammatory responses (8, 10, 13, 14). Leveraging an endothelialized microfluidic model of multiple geometries, Mannino et al. (15) found that VCAM-1 and E-selectin expression, biomarkers of endothelial cell dysfunction, significantly correlated with shear stress variation and were most pronounced near bifurcation points. Furthermore, they found that endothelial cells exposed to SCD RBCs exhibited increased endothelial inflammation

along the outside wall of the bend in the curved regions of vessels (16). These observations indicate that it is essential to understand the role of vascular geometric complexity on endothelial dysfunction in blood disorders.

Aberrant RBCs arising in blood disorders often have very different physical properties compared to healthy RBCs. A typical example is SCD, in which abnormal sickle hemoglobin polymerizes within RBCs upon deoxygenation, creating long fibers that pathologically disrupt cellular architecture (17), leading to increased membrane stiffness as well as loss of cellular volume secondary via dehydration. Subsequently, sickle RBCs are biophysically less deformable than normal cells and some subpopulations are distorted irreversibly into a sickle-like shape. Similarly, in samples of blood from IDA patients, Caruso et al. (18) identified a subpopulation of very small and poorly deformable iron deficiency RBCs (idRBCs). When exposed to COVID-19, morphologically normal RBCs exhibited a conformational change to sphero-echinocytes with reduced size and deformability (2). Relatedly, plasma from adult COVID-19 patients causes substantial RBC aggregation under ow, and brinogen-mediated aggregation directly damages the endothelial glycocalyx (3). In hereditary spherocytosis (HS), genetic mutations affect RBC membrane proteins, breaking the linkage between the membrane skeleton and the lipid bilayer, causing membrane loss (6). As a result, instead of being biconcave discoids, RBCs become inflexible spherical cells called spherocytes.

The spatial distribution of the different cellular components of blood is nontrivial and depends on the relative physical properties of the different components. Normal RBCs migrate toward the center of a blood vessel, leaving an RBC-depleted cell-free layer (CFL) near vessel walls. In contrast, white blood cells (WBCs) and platelets tend to reside in these layers, a flow-induced segregation phenomenon called margination (19–21). Experimental observations of modifications to cell segregation in disease are rare. Observing the flow of suspensions comprised of SCD RBC populations of two different densities, Clavería et al. (22) investi-

gated whether segregation occurs among SCD RBCs flowing in micron-sized channels. It is known (23) that SCD RBCs with higher density exhibited greater shear modulus and, consequently increased rigidity. Clavería et al. found a heterogeneous distribution of SCD RBC according to their density: low-density SCD RBC population remained closer to the center of the channel, while the densest (i.e. stiffest) cells were segregated towards the walls.

The segregation behavior during blood flow is substantially dictated by the contrasts in the cellular properties, such as shape, size, and deformability, of the various components. Kumar et al. (24, 25) used detailed simulations to probe the effect of rigidity difference in a binary suspension of deformable capsules in shear flow. They found that stiff capsules display substantial margination when they are the dilute component, while flexible capsules tend to enrich around the channel's centerline. Similarly, in a mixture of large and small capsules,the smaller capsules marginate (25). Sinha et al. (26) investigated the flow-induced segregation behavior in binary suspensions of spherical and ellipsoidal capsules in simple shear flow by varying the aspect ratio while keeping constant either the equatorial radius or volume of capsules. Direct simulations with models of blood corroborate these model results (27, 28). A simple theory of margination based on the two key transport mechanisms of cells in flow – cell-cell collisions and hydrodynamic migration of deformable cells away from walls (29, 30) predicts that a subpopulation of rigid particles in a suspension of primarily deformable particles, will strongly concentrate at walls during flow (31, 32).

Margination may have particular significance in the context of vasculopathy in blood cell disorders. Endothelial cells are responsible for translating biophysical cues, such as the shear force of the hemodynamic microenvironment, into cellular biological signals (11,33,34). Pathological alterations of such forces promote endothelial activation with the release of proinflammatory signals (35–37), which contribute to atherosclerotic plaques susceptible to myocardial infarction and strokes (38). Indeed, the fact that vasculopathy pervasively occurs even in the

oxygenated conditions in both small and larger vessels demands a new understanding of SCD pathophysiology in the absence of vaso-occlusion, which occurs only under the deoxygenated conditions in the microvessels.

Inspired by advances in the mechanistic understanding of the distribution and segregation behaviors during blood flow as well as experimental observations of blood disorders during flow (15, 16, 18, 22, 39), we propose a biophysical hypothesis for the pathophysiology of vasculopathy in blood disorders: diseased cells strongly marginate, residing primarily in the CFL near the vascular walls, resulting in endothelial inflammation by provoking fluctuations in local wall shear stress, which is consistent with the chronic and diffusive nature of vasculopathy in blood cell disorders. Limited computational studies of this hypothesis, for blood flow in straight tubes, have been performed for the cases of SCD (40) and IDA (18).

The present work uses detailed simulations of a cellular-scale mathematical model of blood flow in small vessels to examine this hypothesis. Several diseases are considered: SCD, IDA, COVID-19, and spherocytosis, in both a simple cylindrical blood vessel geometry and a more geometrically complex serpentine curved tube. The choice of these disease models arose from a number of considerations. On biophysical grounds, all of these disorders result in subpopulations of red cells with altered physical, morphological, and geometric properties. Biologically, they represent a spectrum of disorders that encompass different etiologies, illustrating the generalizability of our findings: SCD arises from a genetic disorder, iron deficiency anemia a nutritional one; COVID-19 is an example of an infectious disease that gives rise to biophysically altered red cell subpopulations, and spherocytosis can arise in genetic or acquired disorders. Not only do the results provide strong and broad-based computational support for our hypothesis, but they also begin to reveal transient aspects of the stress environment experienced by endothelial cells as well as the strong spatial variations in this environment engendered by a complex flow geometry.

An important and distinctive aspect of the study is its focus on mechanism. Because the study is computational, we can interrogate the results in exquisite detail, revealing for example not only the presence, but also the physical origin of a strong localization of aberrant cells in specific regions near the walls of a complex blood vessel. Furthermore, as a computational study, it can also avoid factors such as the broad variability in cell properties, which are inevitable in *in vivo* studies and hard to avoid even in carefully designed *in vitro* studies, that can obscure the dominant phenomena.

# **Results**

#### **Model summary**

We simulate a flowing suspension of RBCs, modeled as deformable fluid-filled elastic capsules, in rigid straight and curved cylindrical tubes with diameter  $D=40\mu m$ . Unless otherwise stated, all results are for simulations that have been run to a statistically stationary state. For the blood disease cases, RBC suspensions are modeled as binary mixtures of normal RBCs with aberrant RBCs from different blood disorders (e.g., idRBCs, sickle RBCs, sphero-echinocytes, and spherocytes). In the binary suspensions, the number fraction for normal RBCs is 0.9, and for aberrant RBCs is 0.1. This is a simplification, as in any real blood cell population there will be a distribution of cell properties. A suspension of only normal RBCs, referred to as healthy RBC suspension, is considered as a control. The overall volume fraction (tube hematocrit) is around 20%, consistent with the observed substantial decrease of hematocrit from large vessel to the microcirculation (41, 42). (There is some variation between the cases we consider here because different cell types have different volumes – what we keep constant between cases are number fraction and number density.) The suspending fluid, blood plasma, is considered incompressible and Newtonian with a viscosity of about  $\eta=1.10-1.35$ mPas. The discoid radius a for human RBC is about  $4\mu m$ . The RBC membrane in-plane shear elasticity modulus

 $G \sim 2.5 - 6 \mu {\rm N/m}$ . The deformability of a capsule in the pressure-driven flow is measured by the dimensionless capillary number  $Ca = \eta \dot{\gamma}_w a/G$ . Ca is set to be 1.0 for normal RBCs, which corresponds to  $\dot{\gamma}_w \sim 1000~{\rm s}^{-1}$ .

Increased membrane stiffness has been identified in a range of blood cell disorders. For example, evidence exists that the membrane shear modulus of a typical sickle cell is approximately four times greater than that of a healthy RBC (43). For IDA, measurements indicate the presence of iron deficient RBCs with stiffness up to ten times greater (18). Subpopulations of RBCs with substantially increased membrane stiffness and smaller dimensions have also been found in COVID-19 (2), and spherocytosis (44). Consequently, for the present study the interfacial shear modulus G of aberrant cells is taken to be five times that of normal RBCs. Therefore, Ca for the aberrant RBCs in our study is at most 0.2 times that for normal RBCs.

The spontaneous shape of the RBC membrane is inhomogeneous. Dupire et al. (45) showed that an RBC maintains its biconcave shape even during tank-treading and hypothesizes that this effect might come from anisotropic elastic properties or an inhomogeneous natural shape. Fischer et al. (46) found that RBCs have "shape memory", which arises from spatial variations in their natural shape. The choice of the spontaneous shape can strongly affect the stable dynamics of the RBC. Sinha et al. (47) investigate the cell dynamics' dependence on the membrane's spontaneous curvature. They found that an oblate spheroidal spontaneous curvature maintains the dimple of the RBC during tank-treading dynamics and exhibits off-shear-plane, tumbling consistent with the experimental observations of Dupire et al. (45). For a complex structure such as an RBC membrane, it is possible that the natural shape for shear elasticity may differ from that for bending elasticity so the overall natural shape of an element results from the balance of bending and shear forces. Thus in this work, the spontaneous shape of RBC bending elasticity is taken to be the oblate spheroid, while the spontaneous shape of RBC shear elasticity is assumed to be the biconcave discoid. Further details are included in the Materials and Methods

section and Supplementary Information; in particular we show that the results here are robust against changes in the details of the cell elasticity model.

#### Cylindrical blood vessel

Figures 1.(A-D) show snapshots from simulations of blood flow in a straight tube for SCD, IDA, COVID-19, and spherocytosis, respectively. (The SI contains movies of these simulations.) In all cases, the aberrant cells (blue) appear to be marginated. Fig.1.(E-H), respectively, show the corresponding radial hematocrit profiles. These indicate that aberrant RBCs strongly marginate, while the normal RBCs display the expected CFL, and a concentration that increases toward the centerline. Sample simulations with doubled tube length and the same mesh spacing were also conducted; changes in the results were negligible. These results demonstrate that differences in cell size and deformability of the aberrant cells are sufficient to drive strong segregation behavior.

The presence of stiff and/or small aberrant cells near vessel walls is expected to generate high velocity gradients, and consequently large shear stresses on the walls,  $\tau_w$ . Fig.2 (A,B,C,D) shows snapshots of the spatial distribution of excess wall shear stress  $\hat{\tau}_w$  for the four cases. Here  $\hat{\tau}_w = \tau_w - \bar{\tau}_w$  is defined as deviation from the mean wall shear stress  $\bar{\tau}_w$ . The red regions indicate large local fluctuations, and one can see that these are directly associated with nearby aberrant RBCs. Fig.2(E) shows time series of additional wall shear stress  $\hat{\tau}_w$  at a point on the wall for the various cases. Peaks of high additional wall shear stress are larger and more frequent in all of the disease cases than in the healthy case. These differences are further quantified in Fig.2(F), which shows the probability density profiles of excess wall shear stress in the suspensions. The PDFs for all aberrant RBC cases display a long tail at high  $\hat{\tau}_w$ , where the probability density of high wall shear stress for cases with aberrant RBCs is orders of magnitude higher than for the healthy case. This phenomenon is especially prominent for

sphero-echinocytes and sickle RBCs and less pronounced with spherocytes, and is related to their morphology: the spiked surfaces of sphero-echinocytes and sickle RBCs induce high local wall shear stress, while the round spherocytes, though near the wall, roll smoothly without generating substantial excess stress.

The simulation findings here are further compared with previous experimental observations in Fig.2(G). To investigate the role of cellular interaction in hematological diseases, Caruso et al. (39) developed an *in vitro* microvasculature model comprised of endothelial cells cultured through the inner surface of a microfluidic system. SCD RBCs were spiked into normal RBC suspension, suspended, and then perfused into this endothelialized microfluidics. They found, VCAM1, a biomarker of endothelial cell dysfunction, was upregulated when exposed to flowing SCD RBCs than normal RBCs. These results together imply that purely physical interactions between endothelial cells and SCD RBCs are sufficient to cause endothelial inflammation.

Moreover, recent research further corroborates our current observations. Specifically, in the context of diabetes-associated oxidative stress leading to reduced RBC deformability, Czaja et al. (49) employed simulations to investigate pulsatile blood flow through segmented retinal microaneurysms. Their findings revealed that diabetic RBCs, characterized by increased stiffness, induced higher local wall stress and wall shear stress gradients within leading and draining parental vessels, compared to their healthy RBC counterparts. Additionally, leveraging a high-fidelity computational model of blood flow, Ebrahimi et al. (50) revealed that reduced cell deformability causes substantial changes in microvascular hemodynamics, and alteration in RBC dynamics induces localized changes in wall shear stress within vessels and in proximity to vascular bifurcations. However, these investigations, while addressing the influence of blood cell deformability on hemodynamics and wall shear stress, did not incorporate the RBC margination driven by deformability difference as a potential contributor to vascular wall stress fluctuations.

#### **Curved blood vessel**

We now consider cell and stress distributions in a curved tube. Fig.3 presents simulation results for a suspension of normal RBCs with sickle RBCs. Snapshots of cell distributions are shown in Fig.3.(A, B), along with a coordinate system we use for the analysis. Fig.3. (C, E), show cell number density distributions for the (C) normal and (E) aberrant cells on the center plane of the channel. The margination of the aberrant cells is apparent. Fig.3.(D, F) show the number density distributions for the normal and aberrant cells averaged over various segments of the channel, including both the normalized center-plane and cross-sectional cell distributions. Fig.3.(D) shows that the CFL thickness is larger near the outer side  $(\theta = 0^{\circ})$  and thinnest near the inner side  $(\theta = 180^{\circ})$ . Fig.3.(F) indicates that sickle RBCs strongly focus at two near-wall locations, both at the inner and outer sides, on the centerplane. As the angle  $\phi$  increases (i.e. as we move downstream around a bend), the concentration of sickle cells near the outer wall becomes more pronounced. Similar results are found for the other aberrant cell suspensions as well, as seen in the cross-sectional and centerplane distributions shown in Fig.S11 in SI.

These results demonstrate that in the curved tube, not only do we see margination of aberrant cells as found in the straight tube, but very strong localization of the marginated cells on the centerplane. The mechanism of this localization originates in the  $\theta$ -dependence of the cell-free layer thickness, as illustrated in Fig. **4**. Fig.**4**.(A) shows a simulation snapshot of cross-section cell distribution at  $\phi = \pi/2$ , in which aberrant cells are highly localized near the outer side centerplane. We noted above that the CFL thickness is approximately uniform for  $\pi/2 < \theta < 3\pi/2 - i.e.$  along the inner wall, but on the outer side, the CFL thickness increases, reaching a maximum on the centerplane on the outer wall – i.e. the CFL thickness increases as  $\theta \to 0$ . A marginated cell on the outer wall will experience more collisions from the side with the thinner CFL than the thicker, thus being driven on average toward the region where the CFL is thickest,  $\theta = 0$ . Fig.**4**.(B) shows the trajectories of marginated aberrant RBCs on the  $\theta - \phi$ 

plane, demonstrating that as  $\phi$  increases,  $\theta$  tends to decrease and aberrant cells move towards the centerplane. We illustrate this mechanism schematically in Fig.4.(C). Finally, we must address why there is localization along the centerplane on the inner wall ( $\theta = \pi$ ). This results from the simple fact that the outer wall over half a wavelength of the curved shape is the inner wall over the other half; the CFL thickness is nearly constant along the inner wall, driving no net motion in  $\theta$ , and cells driven toward  $\theta = 0$  on the outer wall tend to remain there while moving along the inner wall.

Fig.5.(A) shows snapshots of the spatial distribution of excess wall shear stress  $\hat{\tau}_w$  in SCD suspensions; results for the other blood disorders can be found in Fig.S12, S13, S14 in SI. The presence of a sickle RBC close to the wall directly causes local fluctuations in wall shear stress, as can be observed from the transparent view in Fig.5.(B).

To capture the spatial dependence of RBC-induced wall shear stress  $\hat{\tau}_w$ , the probability density profiles of  $\tau_w$  in SCD and healthy RBC suspensions over the different  $\theta$ -areas on the vascular surface are presented in Fig.5.(C). In the healthy RBC suspension, the probability of high  $\hat{\tau}_w$  is largest near the inner side  $(3\pi/4 < \theta < \pi)$ , followed by the intermediate area of  $(\pi/4 < \theta < 3\pi/4)$ , and smallest over the outer side  $(0 < \theta < \pi/4)$ , consistent with the fact that the CFL is thinnest near the inner side and thickest near the outer side. As in the straight tube, it is observed that the cases with aberrant RBCs exhibit a distinct excess of large positive fluctuations, again attributable to the margination of these small stiff cells to the vessel wall. Furthermore, the disparity at high RBC-induced wall shear stress  $\hat{\tau}_w$  of the probability distribution profiles between diseased and healthy RBC suspensions is most pronounced at the outer side, which implies that the localization of the marginated aberrant RBCs to the center plane elevates the probability of high additional wall shear stress by an order of magnitude over the outer side wall of the curved tube.

The geometries of blood vessels have been found to play a role in the development of en-

dothelial dysfunction in blood disorders. Using an endothelialized microfluidic model, Wang et al. (16) discovered that endothelial cells exposed to SCD RBCs exhibited an increase in endothelial inflammation along the outside wall of the bend in the curved regions of vessels. This result is illustrated in Fig.5.(D), which shows expression levels of E-selectin, which is upregulated when cells are in a pro-inflammatory state, upstream and in a curved segment of endothelialized microfluidic channels through which RBC suspensions have flowed. While the channel sizes in the experiments are much larger than those simulated here, the qualitative pattern of endothelial inflammation there is consistent with the margination patterns we observe here.

To further quantify the cellular segregation in different geometries, we measure the scaled root-mean-square (RMS) distance from the centerline,  $s = \langle r_{\rm cm}^2 \rangle^{1/2}/a$ , for each cellular component in straight and curved channels. At the start of the simulations, all cells are randomly distributed within the vascular channels. Fig.6 illustrates the temporal evolution of s for both normal and sickle RBCs. Initially, the aberrant RBCs show a sharp increase in s, then plateau with  $s \approx 3.8$ ; in contrast, for normal cells  $s \approx 2.9$ . This behavior is similar in both straight and curved channels, consistent with the above observations that aberrant cells are localized to vessel walls. Here we have measured time in terms of strain units  $\dot{\gamma}_w t$ , and Fig.6 indicates that, for margination under the present conditions,  $\sim 200$  strain units are required for margination. This can be translated roughly into downstream distance by noting that the mean velocity for laminar flow with wall shear rate  $\dot{\gamma}_w$  is  $\dot{\gamma}_w R$ . Thus in the time of about 200 strain units required for margination to take place, a cell moving at the mean velocity travels 2mm.

Additionally, we observe that segregation occurs somewhat more rapidly in the curved channel compared to the straight channel, as indicated by the faster growth of s for aberrant cells after the simulation starts. While we are unaware of other work on margination in serpentine geometries, relatedly, Bächer et al. (51) explored the margination of microparticles in blood

flow through bifurcations within vascular networks. They found that bifurcations did not substantially influence the margination propensity of stiff particles relative to flow in straight tubes.

### **Discussion**

Blood disorders lead to changes in red blood cell size, shape, and stiffness, and thus to changes in how aberrant cells are distributed in the cross-section of blood vessels, and changes in the interaction between cells and blood vessels. Inflammation and dysfunction of endothelial cells lining blood vessels are associated with the risk of pathophysiologic complications like stroke and atherosclerosis.

This study describes results from detailed cell-level simulations of blood in straight and serpentine tubes, addressing the hypothesis that the margination of aberrant cells leads to substantial changes in the local shear stress environment of the blood vessel wall, possibly contributing to the observed dysfunction and inflammation. We compare cell distributions and wall shear stress profiles between suspensions of normal blood and blood containing aberrant RBCs that model sickle cell disease (SCD), iron deficiency anemia, COVID-19, and spherocytosis. In all cases, the smaller and stiffer aberrant RBCs marginate and increase the fluctuations in wall shear stress. Probability density profiles of wall shear stress show that cases with aberrant RBCs display a significantly higher probability of high wall shear stress than in suspensions of healthy cells. The difference is most notable in COVID-19 and SCD RBC suspensions.

In the serpentine curved tube case, the marginated aberrant cells tend to marginate most strongly to the symmetry plane of the channel and the outer side of the curved tube, becoming very strongly localized in those regions. This result implies the possibility of strongly localized endothelial damage in blood vessels with complex geometries. These findings highlight the importance of considering vascular geometry and the presence of aberrant RBCs in the

development of vasculopathy.

Overall, our study indicates that the biophysical alterations of red cells in various disorders, in and of themselves, can directly alter the shear stress the underlying endothelium is exposed to. This suggests that that red cell biophysics and the pathologic changes thereof may directly affect endothelial mechanobiological pathways, which, in turn, may be associated with chronic endothelial inflammation or dysfunction that lead to disorders such cardiovascular disease and stroke. Experiments to complement these computational results are now being conducted in our group. In addition, our study also suggests that clinically, more attention should be paid to the biophysical alterations of the red cells themselves, which currently are viewed as hallmarks of the associated disease but not necessarily as biomarkers per se; our work suggests otherwise and indicates that the red cell shape, size, deformability should be re-examined more rigorously as potential correlates or predictors of clinical endpoints. Finally, our work indicates that therapeutic interventions that fix or remove the biophysical alterations of red cells should be explored for the associated diseases. Indeed red cell pheresis for various hematology conditions may improve the vascular dysfunction associated with those diseases and for sickle cell disease in particular, recently FDA-approved treatments that improve red cell health may also alleviate vasculopathy.

# **Materials and Methods**

We consider a flowing suspension of RBCs, which we model as deformable fluid-filled elastic capsules, in rigid straight (Fig.1) and curved "serpentine" (Fig.3) cylindrical tubes with radius  $R=20\mu\mathrm{m}$ . No-slip boundary conditions are imposed on the walls of the tube, while periodic boundary conditions are applied in the flow direction. The suspension is subjected to a unidirectional pressure-driven flow, and the velocity field in the absence of RBCs field within the straight cylindrical tube is given by the Poiseuille flow. In this study, the flow is driven by a con-

stant pressure gradient, which is equivalent to fixing the mean wall shear rate at  $\dot{\gamma}_w = 2U_0/R$ , where  $U_0$  is the undisturbed centerline velocity. For the curved cylindrical channel, the pressure gradients are determined using defining an equivalent straight cylindrical channel with the same centerline length and radius.

This study considers both homogeneous and heterogeneous suspensions of various components, including normal RBCs and aberrant RBCs (e.g., iron deficiency RBCs, sickle RBCs, sphero-echinocytes, and spherocytes). In binary suspensions, normal RBCs are generally considered primary components (denoted as "p"), while aberrant RBCs as trace components (denoted as "t"). A normal RBC is modeled as a flexible capsule having the spontaneous shape being a biconcave discoidal for shear elasticity and an oblate spheroid for bending elasticity (47, 52), with a radius of  $a = 4\mu m$ . The idRBCs have the same rest shape as normal RBCs, except the radius of idRBCs is 0.76a (18). The rest shapes of sickle RBCs, spherocytes, and sphero-echinocytes are curved oblate, spherical with a diameter of  $5\mu m$ , and spiked spherical, respectively. The cell membranes are modeled as an isotropic and hyperelastic surface with interfacial shear modulus G, incorporating shear elasticity, area dilatation, volume conservation, and bending resistance. Details of the membrane mechanics model and validation against experimental observations are given in (47).

The deformability of a capsule in pressure-driven flow is measured by the dimensionless capillary number  $Ca = \eta \dot{\gamma}_w a/G$ . In this study, G of the aberrant RBCs is assumed to be five times that of normal RBCs, which leads to that  $Ca_t$  for aberrant RBCs is always around less 0.2 times that of  $Ca_p$  for biconcave discoid RBCs. In this study,  $Ca_p$  is set to 1.0 for normal RBCs,  $Ca_t$  is 0.15 for idRBCs, 0.20 for sickle RBCs, 0.15 for sphero-echinocytes, and 0.125 for spherocytes, which corresponds to  $\dot{\gamma}_w \sim 1000 \, \mathrm{s}^{-1}$ . In the binary suspension, the number fractions for normal RBCs  $X_b$  is set to 0.9, and for aberrant RBCs,  $X_t$  is 0.1, so the overall number density ratio  $n_p/n_t = 9$ . In this study, the total cell volume fraction (hematocrit) is set

to be  $\phi \approx 0.20$ . To simplify the computations in this initial study, the suspending fluid and the fluid inside the cells are assumed to have the same viscosity.

In our simulation, the particle Reynolds number, defined as  $Re_p = \rho \dot{\gamma}_w a^2/\eta$ , is set to be 0.1, and the fluid is assumed to be incompressible and Newtonian; therefore the flow is governed by the Navier-Stokes and continuity equations. A projection method is used to advance the velocity field in time. The straight tube is embedded in a cuboidal computational domain with the size of  $10a \times 10a \times 10a$ , and an Eulerian grid of  $100 \times 100 \times 100$  is used. For the serpentine channel case, the cuboidal computational domain's size is  $32a \times 26a \times 10a$ , and the Eulerian grid of  $320 \times 260 \times 100$  is used. The immersed boundary method (IBM) is used to handle fluid-structure interaction. Specifically, the current model considers two types of immersed boundaries: deformable moving cellular membranes and rigid nonmoving vascular walls. The capsule membrane is discretized into  $N_{\Delta}$  piecewise flat triangular elements;  $N_{\Delta p} = 1280$  for normal RBC, while  $N_{\Delta t} = 682$  for sickle RBC,  $N_{\Delta t} = 816$  for idRBC,  $N_{\Delta t} = 620$  for spherocytes, and  $N_{\Delta t} = 1134$  for sphero-echinocytes. Different  $N_{\Delta}$  are chosen to ensure that the triangular elements on both capsules are close in size. We use "continuous forcing" IBM and "direct forcing" IBM methods for the RBC membranes and tube wall, respectively. The numerical methodology follows the approach described in (53,54).

Several limitations pertain to the model we employed in this study. Firstly, we assume a viscosity ratio of one between the intercellular matrix and plasma, whereas normal RBCs may exhibit a ratio of up to fifteen (55), and aberrant RBCs may possess even higher ratios. As the RBC ages, the viscosity of the cytosol increases (56). Nonetheless, past research (57) has demonstrated that the dynamics of a single sickle cell remain qualitatively unchanged over a broad range of viscosity ratio. Additionally, Reasor et al. (58) performed simulations to investigate the margination dependence on the viscosity ratio, finding that the cell-free-layer thickness and margination of stiff cellular components remain similar. Another limitation of this

study is the assumption of uniform shape, size, and stiffness within each red cell subpopulation, which we know does not fully account for the inherent diversity in these properties present in real red cell populations (59, 60). Nevertheless, while the physical properties of blood cells exhibit dispersity, the variation of these properties within one cell subpopulation is substantially narrower when compared to the variation between different cell subpopulations (see e.g. (18)). Thus we expect that this simplification does not alter the main conclusions drawn here.

Furthermore, sickle cells display increased adhesiveness to the vascular wall, triggering the vaso-occlusion that is the hallmark of SCD. Claveria et al. (22) underscore the role of cell aggregation in mitigating segregation and amplifying CFL thickness, potentially guarding against vaso-occlusion in sickle cell anemia patients. In the present work, we do not consider intercellular forces such as aggregation and adhesion, for two reasons. First, our focus is the broader issue of the role of margination across blood disorders, not just sickle cell disease. Furthermore, aggregation effects are most prominent at low shear rates,  $\lesssim 10s^{-1}$ , whereas the wall shear rate  $\dot{\gamma}_w$  in our simulation remains substantially higher,  $\sim 1000s^{-1}$ , a condition representative of venules and arterioles.

Finally, endothelial cells exposed to shear stress express an endothelial glycocalyx layer (EGL) that plays a central role in mediating vascular permeability and endothelial anti-inflammatory, antithrombotic, and antiangiogenic properties (61). Notably, EGL disruption occurs in arterial regions exposed to disturbed blood flow, accompanied by elevated oxidative stress leading to atherogenesis (62, 63). Our model, which treats the vascular surface as a non-slip rigid boundary, does not capture the permeability and porosity characteristics of EGL. However, it is important to underscore that the presence of EGL, while affecting interactions of RBC with vessel walls, is not anticipated to significantly impact the margination of aberrant cells, which primarily arises from contrasting cellular properties between aberrant and normal RBCs. In addition, our study focuses on conditions within venules and arterioles, where vessel-cell interactions are

less pronounced compared to the confined spaces of capillaries. Therefore, the limitations of our model do not change the central findings in this research: the aberrant cells strongly marginate, residing primarily in the cell-free layer, and generating physical interactions that damage the endothelium.

# Acknowledgments

#### **Funding**

This work was supported by National Science Foundation grant CBET-2042221 (M.D.G., X.C.), an American Society of Hematology (ASH) Research Training Award for Fellows (RTAF), National Institutes of Health, Institute of Heart, Lung, and Blood (NIH NHLBI) grant T32HL139443 and Pediatric Loan Repayment Program (LRP) Award L40HL149069 (C.C.), National Institutes of Health, National Heart, Lung, and Blood Institute grant R35HL145000 (W.A.L.). The work was performed in part at the Georgia Tech Institute for Electronics and Nanotechnology, a member of the National Nanotechnology Coordinated Infrastructure (NNCI), which is supported by the National Science Foundation grant ECCS-2025462. This work used the Advanced Cyberinfrastructure Coordination Ecosystem: Services & Support (ACCESS). In particular, it used the Expanse system at the San Diego Supercomputing Center (SDSC) through allocation MCB190100.

#### **Author contributions**

CC, WAL, MDG designed research, XC performed research, all authors analyzed data and wrote the paper.

# **Competing interests**

The authors declare no competing interests.

# Data availability

All data needed to evaluate the conclusions in the paper are present in the paper and/or the Supplementary Materials.

# **Supplementary Materials**

Materials and Methods

Supplementary Text

Figs. S1 to S14

Movies S1 to S8

Supplementary References (64-87)

# References

- D. C. Rees, T. N. Williams, M. T. Gladwin, Sickle-cell disease. *Lancet* 376, 2018–2031 (2010).
- S. M. Recktenwald, G. Simionato, M. G. Lopes, F. Gamboni, M. Dzieciatkowska, P. Meybohm, K. Zacharowski, A. von Knethen, C. Wagner, L. Kaestner, A. D'Alessandro, S. Quint, Cross-talk between red blood cells and plasma influences blood flow and omics phenotypes in severe COVID-19. *eLife* 11, e81316 (2022).
- S. Druzak, E. Iffrig, B. R. Roberts, T. Zhang, K. S. Fibben, Y. Sakurai, H. P. Verkerke, C. A. Rostad, A. Chahroudi, F. Schneider, A. K. H. Wong, A. M. Roberts, J. D. Chandler, S. O. Kim, M. Mosunjac, M. Mosunjac, R. Geller, I. Albizua, S. R. Stowell, C. M. Arthur, E. J. Anderson, A. A. Ivanova, J. Ahn, X. Liu, K. Maner-Smith, T. Bowen, M. Paiardini, S. E. Bosinger, J. D. Roback, D. A. Kulpa, G. Silvestri, W. A. Lam, E. A. Ortlund, C. L. Maier,

- Multiplatform analyses reveal distinct drivers of systemic pathogenesis in adult versus pediatric severe acute COVID-19. *Nat. Commun.* **14**, 1638 (2023).
- 4. J. M. O'Brien Jr, N. A. Ali, S. K. Aberegg, E. Abraham, Sepsis. *Am. J. Med.* **120**, 1012–1022 (2007).
- 5. S. Von Haehling, E. A. Jankowska, D. J. Van Veldhuisen, P. Ponikowski, S. D. Anker, Iron deficiency and cardiovascular disease. *Nat. Rev. Cardiol.* **12**, 659–669 (2015).
- S. Perrotta, P. G. Gallagher, N. Mohandas, Hereditary spherocytosis. *Lancet* 372, 1411–1426 (2008).
- 7. C. Hahn, M. A. Schwartz, Mechanotransduction in vascular physiology and atherogenesis. *Nat. Rev. Mol. Cell Biol.* **10**, 53–62 (2009).
- 8. B. K. Walther, N. K. R. Pandian, K. A. Gold, E. S. Kiliç, V. Sama, J. Gu, A. K. Gaharwar, A. Guiseppi-Elie, J. P. Cooke, A. Jain, Mechanotransduction-on-chip: vessel-chip model of endothelial YAP mechanobiology reveals matrix stiffness impedes shear response. *Lab Chip* 21, 1738–1751 (2021).
- 9. K.-C. Wang, Y.-T. Yeh, P. Nguyen, E. Limqueco, J. Lopez, S. Thorossian, K.-L. Guan, Y.-S. J. Li, S. Chien, Flow-dependent YAP/TAZ activities regulate endothelial phenotypes and atherosclerosis. *Proc. Natl. Acad. Sci. U.S.A.* **113**, 11525–11530 (2016).
- 10. M. He, M. Martin, T. Marin, Z. Chen, B. Gongol, Endothelial mechanobiology. *APL Bioeng.* **4**, 010904 (2020).
- 11. T. Panciera, L. Azzolin, M. Cordenonsi, S. Piccolo, Mechanobiology of YAP and TAZ in physiology and disease. *Nat. Rev. Mol. Cell Biol.* **18**, 758–770 (2017).

- 12. X. Zhou, W. Xu, Y. Xu, Z. Qian, Iron supplementation improves cardiovascular outcomes in patients with heart failure. *Am. J. Med.* **132**, 955–963 (2019).
- C. Souilhol, J. Serbanovic-Canic, M. Fragiadaki, T. J. Chico, V. Ridger, H. Roddie, P. C. Evans, Endothelial responses to shear stress in atherosclerosis: a novel role for developmental genes. *Nat. Rev. Cardiol.* 17, 52–63 (2020).
- E. Tzima, M. Irani-Tehrani, W. B. Kiosses, E. Dejana, D. A. Schultz, B. Engelhardt, G. Cao,
   H. DeLisser, M. A. Schwartz, A mechanosensory complex that mediates the endothelial cell response to fluid shear stress. *Nature* 437, 426–431 (2005).
- R. Mannino, D. R. Myers, B. Ahn, H. Gole, Y. Wang, A. Lin, R. Guldberg, D. Giddens, L. Timmins, W. A. Lam, Vascular geometry and flow profile mediate pathological cellcell interactions in sickle cell disease as measured with "do-it-yourself" "endothelialized" microfluidics. *Blood* 124, 454 (2014).
- Y. Wang, R. G. Mannino, D. R. Myers, W. Li, C. H. Joiner, W. A. Lam, Vessel geometry interacts with red blood cell stiffness to promote endothelial dysfunction in sickle cell disease. *Blood* 126, 965 (2015).
- 17. J. F. Bertles, P. F. Milner, Irreversibly sickled erythrocytes: a consequence of the heterogeneous distribution of hemoglobin types in sickle-cell anemia. *J. Clin. Investig.* **47**, 1731–1741 (1968).
- 18. C. Caruso, M. E. Fay, X. Cheng, A. Y. Liu, S. I. Park, T. A. Sulchek, M. D. Graham, W. A. Lam, Pathologic mechanobiological interactions between red blood cells and endothelial cells directly induce vasculopathy in iron deficiency anemia. *iScience* 25, 104606 (2022).
- 19. J. C. Firrell, H. H. Lipowsky, Leukocyte margination and deformation in mesenteric venules of rat. *Am. J. Physiol. Heart Circ. Physiol.* **256**, H1667–H1674 (1989).

- 20. G. J. Tangelder, H. C. Teirlinck, D. W. Slaaf, R. S. Reneman, Distribution of blood platelets flowing in arterioles. *Am. J. Physiol. Heart Circ. Physiol.* **248**, H318–H323 (1985).
- J. J. Bishop, A. S. Popel, M. Intaglietta, P. C. Johnson, Effect of aggregation and shear rate on the dispersion of red blood cells flowing in venules. *Am. J. Physiol. Heart Circ. Physiol.* 283, H1985–H1996 (2002).
- V. Clavería, P. Connes, L. Lanotte, C. Renoux, P. Joly, R. Fort, A. Gauthier, C. Wagner,
   M. Abkarian, In vitro red blood cell segregation in sickle cell anemia. *Front. Phys.* 9, 712 (2021).
- E. Evans, N. Mohandas, A. Leung, Static and dynamic rigidities of normal and sickle erythrocytes. Major influence of cell hemoglobin concentration. *J. Clin. Investig.* 73, 477–488 (1984).
- 24. A. Kumar, M. D. Graham, Segregation by membrane rigidity in flowing binary suspensions of elastic capsules. *Phys. Rev. E.* **84**, 066316 (2011).
- A. Kumar, R. G. H. Rivera, M. D. Graham, Flow-induced segregation in confined multicomponent suspensions: effects of particle size and rigidity. *J. Fluid Mech.* 738, 423–462 (2014).
- 26. K. Sinha, M. D. Graham, Shape-mediated margination and demargination in flowing multicomponent suspensions of deformable capsules. *Soft Matter* **12**, 1683–1700 (2016).
- 27. Q. M. Qi, E. S. G. Shaqfeh, Theory to predict particle migration and margination in the pressure-driven channel flow of blood. *Phys. Rev. Fluids* **2**, 093102 (2017).
- 28. K. Mueller, D. A. Fedosov, G. Gompper, Understanding particle margination in blood flow A step toward optimized drug delivery systems. *Med. Eng. Phys.* **38**, 2 10 (2016-01).

- 29. A. Kumar, M. D. Graham, Mechanism of margination in confined flows of blood and other multicomponent suspensions. *Phys. Rev. Lett.* **109**, 108102 (2012).
- V. Narsimhan, H. Zhao, E. S. G. Shaqfeh, Coarse-grained theory to predict the concentration distribution of red blood cells in wall-bounded Couette flow at zero Reynolds number. *Phys. Fluids* 25, 061901 (2013).
- 31. R. G. H. Rivera, K. Sinha, M. D. Graham, Margination regimes and drainage transition in confined multicomponent suspensions. *Phys. Rev. Lett.* **114**, 188101 (2015).
- 32. R. G. H. Rivera, X. Zhang, M. D. Graham, Mechanistic theory of margination and flow-induced segregation in confined multicomponent suspensions: Simple shear and poiseuille flows. *Phys. Rev. Fluids* **1**, 060501 (2016).
- 33. C. Collins, L. D. Osborne, C. Guilluy, Z. Chen, E. T. O'Brien III, J. S. Reader, K. Burridge, R. Superfine, E. Tzima, Haemodynamic and extracellular matrix cues regulate the mechanical phenotype and stiffness of aortic endothelial cells. *Nat. Commun.* **5**, 3984 (2014).
- 34. J. Eyckmans, T. Boudou, X. Yu, C. S. Chen, A hitchhiker's guide to mechanobiology. *Dev. Cell* **21**, 35–47 (2011).
- 35. D. Harrison, J. Widder, I. Grumbach, W. Chen, M. Weber, C. Searles, Endothelial mechanotransduction, nitric oxide and vascular inflammation. *J. Intern. Med.* **259**, 351–363 (2006).
- 36. D. E. Ingber, From mechanobiology to developmentally inspired engineering. *Philos. Trans. R. Soc. Lond., B, Biol. Sci.* **373**, 20170323 (2018).
- 37. D. Ingber, Mechanobiology and diseases of mechanotransduction. *Ann. Med.* **35**, 564–577 (2003).

- 38. J.-i. Abe, B. C. Berk, Novel mechanisms of endothelial mechanotransduction. *Arterioscler. Thromb. Vasc. Biol.* **34**, 2378–2386 (2014).
- C. Caruso, X. Zhang, Y. Sakurai, W. Li, M. E. Fay, M. A. Carden, D. R. Myers, R. G. Mannino, C. H. Joiner, M. D. Graham, W. A. Lam, Stiff erythrocyte subpopulations biomechanically induce endothelial inflammation in sickle cell disease. *Blood* 134, 3560 (2019).
- 40. X. Zhang, C. Caruso, W. A. Lam, M. D. Graham, Flow-induced segregation and dynamics of red blood cells in sickle cell disease. *Phys. Rev. Fluids* **5**, 053101 (2020).
- 41. B. Klitzman, B. R. Duling, Microvascular hematocrit and red cell flow in resting and contracting striated muscle. *Am. J. Physiol. Heart Circ. Physiol.* **237**, H481–H490 (1979).
- 42. I. H. Sarelius, B. R. Duling, Direct measurement of microvessel hematocrit, red cell flux, velocity, and transit time. *Am. J. Physiol. Heart Circ. Physiol.* **243**, H1018–H1026 (1982).
- 43. H. Byun, T. R. Hillman, J. M. Higgins, M. Diez-Silva, Z. Peng, M. Dao, R. R. Dasari, S. Suresh, Y. Park, Optical measurement of biomechanical properties of individual erythrocytes from a sickle cell patient. *Acta Biomater.* **8**, 4130–4138 (2012).
- 44. N. Mohandas, M. R. Clark, M. S. Jacobs, S. B. Shohet, Analysis of factors regulating erythrocyte deformability. *J. Clin. Investig.* **66**, 563–573 (1980).
- 45. J. Dupire, M. Socol, A. Viallat, Full dynamics of a red blood cell in shear flow. *Proc. Natl. Acad. Sci. U.S.A.* **109**, 20808–20813 (2012).
- 46. T. M. Fischer, Shape memory of human red blood cells. *Biophys. J.* **86**, 3304–3313 (2004).
- 47. K. Sinha, M. D. Graham, Dynamics of a single red blood cell in simple shear flow. *Phys. Rev. E.* **92**, 042710 (2015).

- 48. H. Flyvbjerg, H. G. Petersen, Error estimates on averages of correlated data. *J. Chem. Phys.* **91**, 461–466 (1989).
- 49. B. Czaja, J. de Bouter, M. Heisler, G. Závodszky, S. Karst, M. Sarunic, D. Maberley, A. Hoekstra, The effect of stiffened diabetic red blood cells on wall shear stress in a reconstructed 3D microaneurysm. *Comput. Methods Biomech. Biomed. Engin.* 25, 1691–1709 (2022).
- 50. S. Ebrahimi, P. Bagchi, A computational study of red blood cell deformability effect on hemodynamic alteration in capillary vessel networks. *Sci. Rep.* **12**, 4304 (2022).
- C. Bächer, A. Kihm, L. Schrack, L. Kaestner, M. W. Laschke, C. Wagner, S. Gekle, Antimargination of microparticles and platelets in the vicinity of branching vessels. *Biophys. J.* 115, 411–425 (2018).
- 52. E. Evans, Y.-C. Fung, Improved measurements of the erythrocyte geometry. *Microvasc. Res.* **4**, 335–347 (1972).
- 53. P. Balogh, P. Bagchi, A computational approach to modeling cellular-scale blood flow in complex geometry. *J. Comput. Phys.* **334**, 280–307 (2017).
- 54. R. Mittal, H. Dong, M. Bozkurttas, F. Najjar, A. Vargas, A. Von Loebbecke, A versatile sharp interface immersed boundary method for incompressible flows with complex boundaries. *J. Comput. Phys.* **227**, 4825–4852 (2008).
- 55. S. M. Recktenwald, K. Graessel, F. M. Maurer, T. John, S. Gekle, C. Wagner, Red blood cell shape transitions and dynamics in time-dependent capillary flows. *Biophys. J.* **121**, 23–36 (2022).

- M. Nouaman, A. Darras, T. John, G. Simionato, M. A. Rab, R. van Wijk, M. W. Laschke,
   L. Kaestner, C. Wagner, S. M. Recktenwald, Effect of cell age and membrane rigidity on
   red blood cell shape in capillary flow. *Cells* 12, 1529 (2023).
- 57. X. Zhang, W. A. Lam, M. D. Graham, Dynamics of deformable straight and curved prolate capsules in simple shear flow. *Phys. Rev. Fluids* **4**, 043103 (2019).
- 58. D. A. Reasor, M. Mehrabadi, D. N. Ku, C. K. Aidun, Determination of critical parameters in platelet margination. *Ann. Biomed. Eng.* **41**, 238–249 (2013).
- 59. D. Kaul, D. Chen, J. Zhan, Adhesion of sickle cells to vascular endothelium is critically dependent on changes in density and shape of the cells. *Blood* **83**, 3006-3017 (1994).
- 60. G. Nash, C. Johnson, H. Meiselman, Mechanical properties of oxygenated red blood cells in sickle cell (HbSS) disease. *Blood* **63**, 73-82 (1984).
- S. Reitsma, D. W. Slaaf, H. Vink, M. A. Van Zandvoort, M. G. oude Egbrink, The endothelial glycocalyx: composition, functions, and visualization. *Pflügers Arch.* 454, 345–359 (2007).
- 62. G. Dai, S. Vaughn, Y. Zhang, E. T. Wang, G. Garcia-Cardena, M. A. Gimbrone Jr, Biomechanical forces in atherosclerosis-resistant vascular regions regulate endothelial redox balance via phosphoinositol 3-kinase/Akt-dependent activation of Nrf2. *Circ. Res.* 101, 723–733 (2007).
- 63. S. R. McSweeney, E. Warabi, R. C. Siow, Nrf2 as an endothelial mechanosensitive transcription factor: going with the flow. *Hypertension* **67**, 20–29 (2016).
- 64. C. Geuzaine, J.-F. Remacle, Gmsh: A 3-D finite element mesh generator with built-in preand post-processing facilities. *Int. J. Numer. Methods Eng.* **79**, 1309–1331 (2009).

- 65. K. C. Ong, M.-C. Lai, Y. Seol, An immersed boundary projection method for incompressible interface simulations in 3D flows. *J. Comput. Phys.* **430**, 110090 (2021).
- 66. P. B. Canham, The minimum energy of bending as a possible explanation of the biconcave shape of the human red blood cell. *J. Theor. Biol.* **26**, 61–81 (1970).
- 67. W. Helfrich, Elastic properties of lipid bilayers: theory and possible experiments. *Z. Natur-forsch. C.* **28**, 693–703 (1973).
- 68. R. Skalak, A. Tozeren, R. Zarda, S. Chien, Strain energy function of red blood cell membranes. *Biophys. J.* **13**, 245–264 (1973).
- G. Tryggvason, B. Bunner, A. Esmaeeli, D. Juric, N. Al-Rawahi, W. Tauber, J. Han, S. Nas, Y.-J. Jan, A front-tracking method for the computations of multiphase flow. *J. Comput. Phys.* 169, 708–759 (2001).
- 70. J. B. Freund, J. Vermot, The wall-stress footprint of blood cells flowing in microvessels. *Biophys. J.* **106**, 752–762 (2014).
- 71. P. Balogh, P. Bagchi, Three-dimensional distribution of wall shear stress and its gradient in red cell-resolved computational modeling of blood flow in in vivo-like microvascular networks. *Physiol. Rep.* **7**, e14067 (2019).
- 72. D.-V. Le, S. T. Wong, A front-tracking method with Catmull–Clark subdivision surfaces for studying liquid capsules enclosed by thin shells in shear flow. *J. Comput. Phys.* **230**, 3538–3555 (2011).
- 73. R. Fahraeus, T. Lindqvist, The viscosity of the blood in narrow capillary tubes. *Am. J. Physiol.* **96**, 562–568 (1931).

- 74. A. R. Pries, D. Neuhaus, P. Gaehtgens, Blood viscosity in tube flow: dependence on diameter and hematocrit. *Am. J. Physiol. Heart Circ. Physiol.* **263**, H1770–H1778 (1992).
- 75. Y. Fung, B. Zweifach, Microcirculation: mechanics of blood flow in capillaries. *Annu. Rev. Fluid Mech.* **3**, 189–210 (1971).
- 76. A. Pries, K. Ley, M. Claassen, P. Gaehtgens, Red cell distribution at microvascular bifurcations. *Microvasc. Res.* **38**, 81–101 (1989).
- 77. C. Dupont, A.-V. Salsac, D. Barthès-Biesel, Off-plane motion of a prolate capsule in shear flow. *J. Fluid Mech.* **721**, 180–198 (2013).
- 78. Z. Wang, Y. Sui, P. D. Spelt, W. Wang, Three-dimensional dynamics of oblate and prolate capsules in shear flow. *Phys. Rev. E.* **88**, 053021 (2013).
- L. Lanotte, J. Mauer, S. Mendez, D. A. Fedosov, J.-M. Fromental, V. Claveria, F. Nicoud, G. Gompper, M. Abkarian, Red cells' dynamic morphologies govern blood shear thinning under microcirculatory flow conditions. *Proc. Natl. Acad. Sci. U.S.A.* 113, 13289–13294 (2016).
- 80. C. Minetti, V. Audemar, T. Podgorski, G. Coupier, Dynamics of a large population of red blood cells under shear flow. *J. Fluid Mech.* **864**, 408–448 (2019).
- 81. D. Cordasco, P. Bagchi, Orbital drift of capsules and red blood cells in shear flow. *Phys. Fluids* **25**, 091902 (2013).
- 82. M. Bitbol, Red blood cell orientation in orbit C = 0. Biophys. J. 49, 1055–1068 (1986).
- 83. Z. Peng, A. Mashayekh, Q. Zhu, Erythrocyte responses in low-shear-rate flows: effects of non-biconcave stress-free state in the cytoskeleton. *J. Fluid Mech.* **742**, 96–118 (2014).

- 84. D. Cordasco, A. Yazdani, P. Bagchi, Comparison of erythrocyte dynamics in shear flow under different stress-free configurations. *Phys. Fluids* **26**, 041902 (2014).
- 85. J. Mauer, S. Mendez, L. Lanotte, F. Nicoud, M. Abkarian, G. Gompper, D. A. Fedosov, Flow-induced transitions of red blood cell shapes under shear. *Phys. Rev. Lett.* **121**, 118103 (2018).
- 86. M. Abkarian, M. Faivre, A. Viallat, Swinging of red blood cells under shear flow. *Phys. Rev. Lett.* **98**, 188302 (2007).
- 87. F. Reichel, J. Mauer, A. A. Nawaz, G. Gompper, J. Guck, D. A. Fedosov, High-throughput microfluidic characterization of erythrocyte shapes and mechanical variability. *Biophys. J.* **117**, 14–24 (2019).

**Fig. 1.** Cell distributions within a cylindrical blood vessel. (Top) Simulation snapshots for (A) sickle cell disease, (B) iron deficiency anemia, (C) COVID-19, and (D) spherocytosis, in straight cylindrical tube subjected to a unidirectional pressure-driven flow. Red capsules represent normal RBCs with oblate spheroid shape for bending elasticity and biconcave discoid shape for shear elasticity, while blue capsules are for aberrant RBCs. (Bottom) Radial hematocrit profile for (red) normal RBCs and (blue) aberrant RBCs of (E) sickle cells in SCD, (F) idRBCs in IDA, (G) sphero-echinocytes in COVID-19, and (H) spherocytes in spherocytosis. In all figures, error bars represent estimated standard error using the block averaging method (48).

Fig. 2. Shear stress on a cylindrical blood vessel. (Top) Simulation snapshots and corresponding transparent views of excess wall shear stress  $\hat{\tau}_w$ , induced by the presence of the cells in (A) sickle cell diseases, (B) iron deficiency anemia, (C) COVID-19, and (D) spherocytosis RBC suspensions. To distinguish the colors of the cells themselves from the colors of the RBC-induced wall shear stress on the cylindrical surface, the color of normal RBCs is set to be pale red, and aberrant RBCs pale blue. (Bottom) (E) Time evolution of the additional wall shear stress  $\hat{\tau}_w$  (i. e. deviation from the mean) at a fixed wall position for the cases of a homogeneous suspension of healthy RBCs and binary suspensions of normal RBCs with aberrant RBCs, respectively. (F) Probability distribution of the additional wall shear stresses  $\hat{\tau}_w$  over the cylindrical wall in the various cases. (G) Endothelial VCAM-1 expression in "endothelialized" microfluidic devices with a width of  $100\mu$ m after perfusion of suspensions with various fractions of (AA) normal and (SS) SCD RBCs (39).

**Fig. 3. Cell distributions within a curved blood vessel.** (A, B) Simulation snapshots of a suspension of normal RBCs with sickle RBCs in a curved channel, showing coordinate def-

initions for r the distance from the local channel centerline,  $\theta$ , the relative position between the "inner side" ( $\theta=180^\circ$ ) and "outer side" ( $\theta=0^\circ$ ), and  $\phi$ , the angle around the curve. (C) Normalized center-plane cell number density and (D) normalized cross-sectional cell number density for normal RBCs in the binary SCD RBC suspension. (E) Normalized center-plane cell number density and (F) normalized cross-sectional cell number density for sickle RBCs in the binary SCD RBC suspension. Note that the curved channel is divided into three parts based on the value of angle  $\phi$ ; thus, the cross-sectional cell number distribution is computed over each part. The cell number density distributions are normalized so that if the spatial distributions of cells is uniform, then the normalized cell number density is unity everywhere within the curved channel.

Fig. 4. Mechanism of cell-localization on the symmetry plane of a curved vessel. (A) Simulation snapshot showing the cross-section cell distribution ( $\phi = \pi/2$ ). (B) Trajectories of sickle RBCs on the  $\theta - \phi$  plane. Dashed blue curves are individual trajectories; the red line denotes the root mean squared trajectory of the blue curves, and the red shaded area is for the corresponding standard deviation. (C) A schematic mechanism for localization of marginated cells to  $\theta = 0$ .

Fig. 5. Shear stress on a curved blood vessel. (A) Simulation snapshots and (B) corresponding transparent views of additional wall shear stress  $\hat{\tau}_w$  induced by the presence of the cells in suspensions of normal RBCs with sickle RBCs within the curved channel. The color on the vascular surface denotes the RBC-induced wall shear stress strength  $\hat{\tau}_w$ . (C) The time-averaged probability distribution of the additional wall shear stress  $\hat{\tau}_w$  for SCD RBC suspension and healthy RBC suspension over the different  $\theta$ -area on the curved vascular surface. (D) Mechanically stiff SCD RBCs upregulate E-selectin at the curvature site of vasculature models,

indicating pro-inflammatory endothelial signaling (16). Scale bars =  $200 \mu m$ 

Fig. 6. Segregation in straight and curved channels. Temporal evolution of RMS distance from the centerline,  $s = \langle r_{\rm cm}^2 \rangle^{1/2}/a$  for each cellular component (red, normal RBCs; blue, aberrant RBCs) in an SCD RBC suspension within the straight tube (solid line) and curved channel (dash line).  $r_{cm}$  is the radial center-of-mass position of a cell and angle brackets denote averaging over the cells in the system. Both the cylindrical straight and curved channels have a tube radius of  $20\mu \rm m$ .

# Supplementary Materials for Marginated aberrant red blood cells induce pathologic vascular stress fluctuations in a computational model of hematologic disorders

Xiaopo Cheng,<sup>1</sup> Christina Caruso,<sup>2</sup> Wilbur A. Lam,<sup>2,3\*</sup> Michael D. Graham<sup>1\*</sup>

<sup>1</sup>Department of Chemical and Biological Engineering, University of Wisconsin-Madison, Madison, WI 53706, USA

<sup>2</sup>Aflac Cancer and Blood Disorders Center of Children's Healthcare of Atlanta,
 Department of Pediatrics, Emory University School of Medicine, Atlanta, GA 30307, USA
 <sup>3</sup>Wallace H. Coulter Department of Biomedical Engineering,
 Georgia Institute of Technology and Emory University, Atlanta, GA 30332, USA

\*To whom correspondence should be addressed; E-mail: wilbur.lam@emory.edu, mdgraham@wisc.edu

# This PDF file includes:

Materials and Methods

Supplementary Text

Figs. S1 to S14

Movies S1 to S8

Supplementary References (64-87)

### **Materials and Methods**

We have developed a computational model utilizing the immersed boundary method (IBM) to investigate cellular blood flow in complex vessel geometries. This approach offers the advantage of modeling flows in arbitrary geometries and accurately resolving the large deformation and dynamics of blood cells. Our model considers blood as a confined flowing suspension of red blood cells (RBCs) in the plasma. Two distinct types of boundaries are involved: deformable cellular membranes and rigid non-moving vascular walls with complex geometry. To handle these two types of interfaces, we use the continuous-forcing and direct-forcing immersed boundary methods, respectively. Specifically, the continuous-forcing IBM method couples surface stresses on the RBC membrane with the fluid flow, while the sharp-interface ghost-node immersed boundary method (GNIBM) is used to treat the rigid, non-moving vascular walls (53, 54). The flow solver is based on a coupled finite-volume/spectral method, and our IBM code is parallelized using a hybrid MPI/OpenMP strategy.

#### **Governing Equations**

Assuming that blood plasma is both Newtonian and incompressible, the governing equations for its flow can be expressed as the incompressible Navier-Stokes equations.

$$Re\left(\frac{\partial \boldsymbol{u}}{\partial t} + \nabla \cdot \boldsymbol{u}\boldsymbol{u}\right) = -\nabla P + \nabla^2 \boldsymbol{u} + \boldsymbol{F}$$

$$\nabla \cdot \boldsymbol{u} = 0$$
(1)

#### **Flow Solver**

The Chorin projection method is utilized to advance the velocity field u. This method involves solving an advection-diffusion equation (ADE) to determine the intermediate velocity field  $u^*$ , followed by solving a Poisson equation for pressure P to enforce the divergence-free

constraints.

$$Re\frac{\boldsymbol{u}^* - \boldsymbol{u}^n}{\Delta t} = \nabla^2 \boldsymbol{u} - Re\nabla \cdot \boldsymbol{u}\boldsymbol{u} + \boldsymbol{F}$$

$$\nabla^2 P = \frac{Re}{\Delta t} \nabla \cdot \boldsymbol{u}^*$$

$$\frac{\boldsymbol{u}^{n+1} - \boldsymbol{u}^*}{\Delta t} = -\frac{1}{Re} \nabla P$$
(2)

For the ADE, we treat both the convection term and the body force term with the 2nd-order Adams-Bashforth method (AB2), and the diffusion term with the Crank-Nicholson method for numerical stability.

$$Re\frac{\mathbf{u}^* - \mathbf{u}^n}{\Delta t} = 0.5\nabla^2(\mathbf{u}^* + \mathbf{u}^n) + 1.5N(\mathbf{u}^n) - 0.5N(\mathbf{u}^{n-1}) + 1.5\mathbf{F}^n - 0.5\mathbf{F}^{n-1}$$
(3)

where  $N(\boldsymbol{u}) = -Re\nabla \cdot \boldsymbol{u}\boldsymbol{u}$  denotes the nonlinear convection, evaluated then by the central differencing. To leverage the efficient inversion of tri-diagonal matrices, a Locally One-Dimensional (LOD) Alternating Direction Implicit (ADI) scheme is employed to solve the ADE. This scheme involves four steps: first, the explicit terms are handled; then, the x, y, and z directions are solved implicitly, one at a time. To solve the 3D pressure Poisson equation (PPE), we assume that the computational domain is periodic in two directions, namely x and y. We begin by performing a 2D fast Fourier transform (FFT) on each x-y plane. Next, solve for the Fourier coefficients along the z direction. Finally, perform a 2D inverse fast Fourier transform (iFFT) on each x-y plane to obtain the pressure field.

#### **Spatial Discretization**

The IBM requires an Eulerian representation for the fluid flow and a Lagrangian representation for the immersed boundaries such as the RBC membrane. The governing equations are solved on the Eulerian grid. To avoid odd-even decoupling, spatial discretization is based on the staggered mesh, in which these scalar variables, such as pressure P, are located at the grid center, while vector variables, such as velocity u and force F, are located at the grid faces. All spatial derivatives are evaluated using second-order differencing. As for the Lagrangian mesh on the

immersed boundaries, the membrane is discretized into piecewise flat triangular elements. An open-source software Gmsh (64) is used to generate the surface mesh for both vessels (Fig. S1.) and various red blood cells (Fig. S2.).

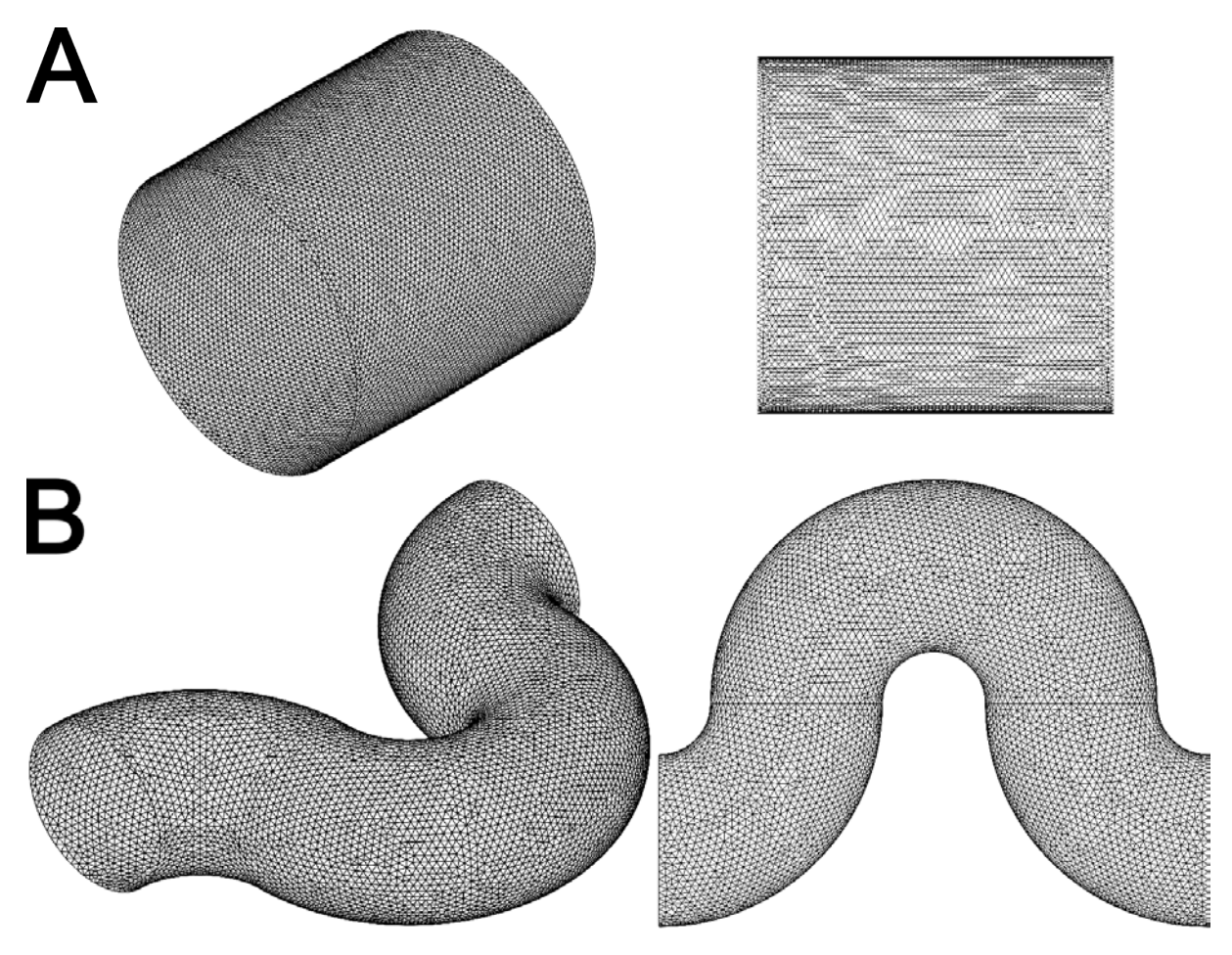


Fig. S1. Surface mesh for (A) a straight cylindrical tube (radius  $R=20\mu m$  and length  $L=40\mu m$ ) and (B) a curved (serpentine) cylindrical channel (major radius  $R_1=32\mu m$  and minor radius  $R_2=20\mu m$ ).

#### **Membrane Mechanics**

The RBC membrane is assumed to resist shear deformation, area dilatation, volume conservation (65), and bending resistance. The total strain energy of the RBC membrane S is given

by,

$$E = \frac{K_B}{2} \int_S (2\kappa_H + c_0)^2 dS + \overline{K_B} \int_S \kappa_G dS + \int_S W dS$$

where  $K_B$  and  $\overline{K_B}$  are the bending moduli, and W is the shear strain energy density;  $\kappa_H$ ,  $\kappa_G$  are the mean and Gaussian curvature of the surface, respectively;  $c_0 = -2H_0$  is the spontaneous curvature, where  $H_0$  is the mean curvature of the spontaneous shape. The first two terms correspond to the Canham-Helfrich bending energy (66,67), and the third term comes from the shear strain energy stored in the RBC membrane. The strain energy density is computed based on the Skalak model (68). A finite element method (FEM) is developed to find the surface stress as a result of membrane deformation (47).

#### **Continuous Forcing IBM**

The cellular membrane is deformed by the fluid flow, while the flow is altered by the membrane deformation in turn. This fluid-structure interaction (FSI) between flow and membrane is characterized via the continuous forcing IBM. The idea of this method is to add an external force term  $\mathbf{F}$  to the right-hand side of the Navier-Stokes equation. The external force term originates from the membrane stress  $f_{\text{membrane}}$ . A discretized delta function is used to spread the singular force on the membrane to the surrounding fluid and interpolate the fluid velocity back to the membrane.

$$F = \int_{S} f_{\text{membrane}} \delta (x - x') dx'$$

$$u_{\text{membrane}} = \int_{\mathcal{T}} u \delta (x' - x) dx$$
(4)

 $\delta$  is the three-dimensional Dirac-delta function, and  $\mathbf{x}$  and  $\mathbf{x}'$  are the locations in the flow domain  $\mathcal{T}$  and on the cell surface S, respectively. A numerical approximation of the delta function is chosen to be

$$\delta(\mathbf{x} - \mathbf{x}') = \begin{cases} \frac{1}{64\Delta^3} \prod_{i=1}^3 \left[ 1 + \cos \frac{\pi}{2\Delta} (x_i - x_i') \right], & |x_i - x_i'| \le 2\Delta \\ 0, & |x_i - x_i'| > 2\Delta \end{cases}$$
 (5)

where  $\Delta$  is the Eulerian grid size.

#### **Direct Forcing IBM**

Direct forcing IBM is used to treat another type of immersed boundary, the rigid, non-moving but geometrically complex vessel walls. Specifically, GNIBM is used to impose no-slip velocity boundary conditions on the vessel surface (54). The idea of this method is to modify these differential operators appropriately to satisfy the no-slip boundaries condition on the geometrically-complex vascular surface while maintaining second-order accuracy.

#### **Indicator Function for Hematocrit Analysis**

To characterize the cellular spatial distribution in RBC suspension, we define an indicator function  $I(\mathbf{x}, t)$ , such that the indicator function is one inside a cell, and zero outside a cell. It can be shown (69) that the indicator function  $I(\mathbf{x}, t)$  follows a Poisson equation as

$$\nabla^2 I = \nabla \cdot \mathbf{G}, \quad \mathbf{G}(\mathbf{x}, t) = \int_S \delta(\mathbf{x} - \mathbf{x}') \,\mathbf{n} dS \tag{6}$$

where the G(x, t) is an Eulerian variable constructed from the cell surface normals n.

#### **Wall Shear Stress Evaluation**

To compute wall shear stress, the traction vector  $\mathbf{t} = \boldsymbol{\tau} \cdot \mathbf{n}$  at the wall is determined using the velocity field approach outlined in (70,71), where  $\boldsymbol{\tau}$  is the stress tensor and  $\boldsymbol{n}$  is the unit normal vector. The no-slip condition on the blood vessel surface yields the expression for the local wall shear stress  $t_s = \mu \partial u_s / \partial r$ . Note s denotes the local stream-wise direction. The second-order differencing method is utilized to numerically evaluate velocity derivatives.

#### Model Verification and Validation

#### **Elastic Spherical Capsule in Simple Shear Flow**

We consider a moving deformable spherical capsule subjected to simple shear flow, see Fig.S3.(A). The deformation of a capsule will cause stretching stress and bending stress on its surface. The deformability of a capsule is characterized by the nondimensional Capillary number  $Ca = \mu \dot{\gamma} a/G$  and the nondimensional bending modulus  $\hat{\kappa}_B = K_B/a^2G$ , where  $\mu$  is the fluid viscosity,  $\dot{\gamma}$  is shear rate, a is the radius of the capsule, G is the shear elasticity modulus and  $K_B$  is the bending modulus. Larger Ca and  $\hat{\kappa}_B$  means that a capsule is more flexible, while a stiffer capsule has smaller Ca and  $\hat{\kappa}_B$ . The deformation of the capsule is described by the Taylor shape parameter defined as  $D_{xz} = (L-B)/(L+B)$ , where L and B are the maximum and minimum radial distances of an ellipsoid with the same inertia tensor. In Fig.S3.(B), we show that steady state values of Taylor deformation parameter D as a function of dimensionless Capillary number Ca for different  $\hat{\kappa}_B$ . Good agreement is found between our numerical results and simulation results from previous literature (72).

#### Stationary Rigid Sphere in Simple Shear Flow

We consider a rigid stationary sphere subjected to a linear shear flow, which is given by  $\mathbf{u}^{\infty} = [\dot{\gamma}z, 0, 0]$ . The schematic of the model set is shown in Fig.S4.(A). The analytical solution for this problem is given by

$$u = \frac{y\dot{\gamma}}{2} \left[ 1 - \left(\frac{r}{a}\right)^{-5} \right] + \frac{y\dot{\gamma}}{2} \left[ 1 - \left(\frac{r}{a}\right)^{-3} \right] - \frac{5}{2} \left(\frac{x}{a}\right)^2 y\dot{\gamma} \left[ \left(\frac{r}{a}\right)^{-5} - \left(\frac{r}{a}\right)^{-7} \right]$$

$$v = \frac{x\dot{\gamma}}{2} \left[ 1 - \left(\frac{r}{a}\right)^{-5} \right] - \frac{x\dot{\gamma}}{2} \left[ 1 - \left(\frac{r}{a}\right)^{-3} \right] - \frac{5}{2} \left(\frac{y}{a}\right)^2 x\dot{\gamma} \left[ \left(\frac{r}{a}\right)^{-5} - \left(\frac{r}{a}\right)^{-7} \right]$$

$$w = -\frac{5}{2} \frac{xyz\dot{\gamma}}{a^2} \left[ \left(\frac{r}{a}\right)^{-5} - \left(\frac{r}{a}\right)^{-7} \right]$$

$$(7)$$

where u, v, w are the velocity component in each dimension,  $r = \sqrt{x^2 + y^2 + z^2}$  is the distance from a point in flow to the center of the sphere, a is the radius of the sphere. Using the direct

forcing IBM, we set the velocity on the sphere surface to zero (no-slip boundary condition). Note the solution above is for unbounded shear flow, thus we impose the Dirichlet velocity boundary conditions on both the upper and bottom walls and choose a larger computation domain to reduce the error by periodic boundaries. After the velocity field reaches its steady state, our numerical results are then compared with the analytical solutions.  $L_1$  and  $L_2$  error norms for different velocity components u, v, w are plotted in Fig.S4.(B). It is found that the direct forcing IBM in our model presents second-order accuracy.

#### Fåhræus-Lindqvist effect: Blood Relative Apparent Viscosity

Fåhræus and Lindqvist (73) made the noteworthy observation that the apparent viscosity at shear rates  $\geq 100~\rm s^{-1}$ , determined using Poiseuille's law in a capillary viscometer, exhibited a strong dependence on the capillary tube diameter. This phenomenon is called the Fåhræus-Lindqvist effect. For large tube diameters, a constant viscosity plateau was evident. But within the range of 10 and  $1000\mu \rm m$ , the apparent viscosity decreases substantially with decreasing tube size, before increasing sharply for tubes smaller than  $10\mu \rm m$ . The increase for very small tubes is readily explained by the relative size of red blood cells, which are approximately  $8\mu \rm m$  in diameter, but the behavior at larger tube diameters is more subtle. In this study, we investigate the behavior of healthy RBCs flowing through tubes of varying radius, ranging from  $R=6\mu m$  to  $R=20\mu m$ , as illustrated in Fig.S5.(A). Then the computed relative apparent viscosity, as a function of tube diameter, is shown in Fig.S5.(B). Fig.S5. indicates that our numerical simulation qualitatively predicts the Fåhræus-Lindqvist effect. For comparison, we also show the empirical relation established by Pries et al (74) based on *in vitro* blood flow. It is found that our model predicts apparent viscosity in good agreement with the empirical relation at the physiological length scales we study in this work.

### **Zweifach-Fung Effect: RBC Partitioning at a Bifurcation**

The partitioning of blood plasma and cells near a vascular bifurcation is complex. In the microcirculation, when RBCs pass through a bifurcating region of a blood vessel, they exhibit a tendency to preferentially flow into the daughter vessel with the higher flow rate, resulting in fewer cells flowing into the vessel with the lower flow rate. This phenomenon, termed the Zweifach-Fung effect (75), plays a crucial role in shaping blood flow distribution within the microvascular network. Here we compare simulation results from our model with experimental observations from previous literature (76). The radius of the inlet vessel is taken to be  $10\mu m$ , in order to be close to the value used in experiments, as shown in Fig.S6. The Zweifach-Fung effect is quantified in Fig.S6.(B). The parameter  $\eta_Q$  is defined to characterize partition as the ratio of the volumetric flow rate at one daughter branch to the volumetric flow rate at the parent vessel. Similarly,  $\eta_N$  is defined as the ratio for cell number flow rate. From the results in Fig.S6., it is found that our simulation results are in good agreement with the experimental findings (76). Further results on the flow of diseased blood in bifurcations and junctions will be reported elsewhere.

## Impact of Membrane Spontaneous Curvature on RBC Dynamics

Although efforts to understand RBC dynamics numerically have spanned the past two decades, the majority of these works have focused on RBC dynamics in cases where the RBC shape is symmetric across the shear plane or where the dimple is centered on the shear plane. Dupont et al. (77) demonstrated that an elastic capsule with a prolate spheroid rest shape, whose axis of symmetry is oriented off the shear plane, will exhibit a unique final dynamical motion for all initial orientations. Depending on the capillary number, they observed three final dynamical states: (i) rolling for lower capillary numbers, (ii) wobbling in which the capsule processes around the vorticity axis as the capillary number is increased, and (iii) a swinging-oscillating

motion in which the long axis of the capsule oscillates around the shear plane with decreasing amplitude of oscillation as the capillary number increases, resulting in an in-plane swinging motion at high capillary numbers. Wang et al. (78) investigated the off-plane motion of oblate and prolate capsules and concluded that the final dynamical state could depend on the initial inclination angle. A recent study of RBCs in shear flow (79) has demonstrated that RBCs first tumble, then roll, transit to a rolling and tumbling stomatocyte, and finally attain polylobed shapes with increasing shear rate when the viscosity contrast between cytosol and blood plasma is large enough. Minetti et al. (80) give an exhaustive description of the dynamics under a shear flow of a large number of RBCs in a dilute regime is proposed. They identify which of the characteristic parameters of motion and of the transition thresholds depend on flow stress only or also on suspending fluid viscosity.

Similarly, Cordosco and Bagchi (81) studied the off-plane motion of oblate, prolate, and biconcave capsules. Unlike Dupont et al. (77) and Wang et al. (78), they included membrane bending stiffness in their formulation and considered a spatially uniform spontaneous curvature in the case of biconcave capsules. They found that rolling was the dominant mode in the physiologically relevant viscosity ratio case (i.e., 5), tank-treading or wobbling mode at  $\lambda < 1$ , and an intermittent regime at low capillary numbers and low viscosity ratios, where the dynamics are dependent on the initial orientation. It is noteworthy that Bitbol (82) and Dupire et al. (77) experimentally observed rolling dynamics in a dextran solution where the viscosity ratio was less than unity. The discrepancy between simulation and experiment may result from the use of a spatially uniform spontaneous curvature that corresponds to a biconcave shape. It is important to note that to model the RBC membrane correctly, an assumption of the spontaneous shape has to be made, and finding the appropriate shape has been a challenge for both theoreticians and experimentalists. Sinha et al. (47) investigate the cell dynamics' dependence on the membrane's spontaneous curvature. They found that an oblate spheroidal spontaneous curvature maintains

the dimple of the RBC during tank-treading dynamics and exhibits off-shear-plane, tumbling consistent with the experimental observations of Dupire et al. (45). For a complex structure such as an RBC membrane, it is possible that the natural shape for shear elasticity may differ from that for bending elasticity so the overall natural shape of an element results from the balance of bending and shear forces.

There have been endeavors to comprehend the impact of spontaneous shape on the ultimate dynamics of RBCs. Peng et al. (83) conducted a study on the influence of non-biconcave spontaneous shape on RBC dynamics and concluded that in order for an RBC to maintain its biconcave shape during tank-treading, as noted by Dupire et al. (45), the spontaneous curvature must be non-biconcave. In instances where a biconcave spontaneous curvature was employed, tank-treading could not be achieved without significantly perturbing the initial shape. Additionally, Cordosco et al. (84) explored non-biconcave spontaneous shapes and ascertained that the spontaneous shape has a significant impact on cell dynamics, depending on the viscosity ratio. They observed that the dimple in the RBC remained intact for both biconcave and oblate spontaneous shapes. However, it should be noted that in both works, Peng et al. (83) and Cordasco et al. (84), non-biconcave spontaneous curvatures were investigated under the imposition of spatially uniform spontaneous curvature, denoted as  $c_0$ . It is worth highlighting that RBC membranes differ from model lipid bilayers in that they possess embedded proteins with an underlying spectrin cytoskeleton and an asymmetric bilayer leaflet composition, all of which modify  $c_0$ , with proteins in particular, having been demonstrated to preferentially bind via curvature-sensing mechanisms. Hence, it can be argued that  $c_0$  would be spatially inhomogeneous. Recently, using two different simulation techniques, Mauer et al. (85) construct a state diagram of RBC shapes and dynamics in shear flow as a function of shear rate and viscosity contrast (45, 86). Their studies suggest that a nearly spherical stress-free shape best reproduces experimental results for the tumbling-to-tank-treading transition at low viscosity contrasts. Reichel et al. (87) combined simulation and experimental investigation of RBC shapes and dynamics in microchannels to provide a consistent RBC state diagram and illustrate the complexity of RBC behavior in the microflow. The RBC model employs a stress-free shape of the elastic spring network, corresponding to a spheroidal shape with a reduced volume of 0.96. Their simulation results agree well with experimental observations, allow the characterization of RBC variability in shear elasticity, and permit us to make a significant step toward quantitative measurements of RBC mechanical properties.

In our work, to investigate the effects of membrane curvature on the RBC dynamics, two types of homogeneous normal RBCs suspension are simulated: one with spontaneous bending curvature being biconcave discoid, while another being oblate spheroid. Various vascular geometries are considered, including a slit (Fig. S7.), a straight cylindrical tube (Fig. S8.), and a curved (serpentine) channel (Fig. S9.). The simulation snapshots tell that RBC rest shape has a nontrivial impact on its near-wall dynamics: RBCs with biconcave discoid rest shape tend to "rolling", while RBCs with oblate spheroid rest shape perform "tank-treading", consistent with the findings in a prior numerical investigation by Sinha et al. (47). In spite of the change in orientational dynamics when the spontaneous shape is changed, no substantial change is observed in the number density distribution for normal RBCs.

## Simulation snapshots of Cell Distributions in Straight Cylindrical Tube

The simulation snapshots showing the segregation phenomenon between normal and aberrant cells in the straight cylindrical tube are given in Fig. **S10.**.

# RBC-induced Local Wall Shear Stress Fluctuation on Curved Channel Surface

Cross-sectional and center-plane normalized cell number density distribution of iron deficiency RBCs, sphero-echinocytes, and spherocytes over the curved channel in each corresponding

binary suspension of normal RBCs with aberrant RBCs are shown in Fig.S11.. Aberrant RBCs margination provokes local wall shear stress fluctuation on curved channel surfaces are shown in Fig. S12., S13., and S14..

## **Movies**

Movie S1.

SCD RBC suspension in Straight Cylindrical Tube

Movie S2.

IDA RBC suspension in Straight Cylindrical Tube

Movie S3.

COVID-19 RBC suspension in Straight Cylindrical Tube

Movie S4.

Spherocytosis RBC suspension in Straight Cylindrical Tube

Movie S5.

SCD RBC suspension in Curved Channel

Movie S6.

IDA RBC suspension in Curved Channel

Movie S7.

COVID-19 RBC suspension in Curved Channel

## Movie S8.

Spherocytosis RBC suspension in Curved Channel

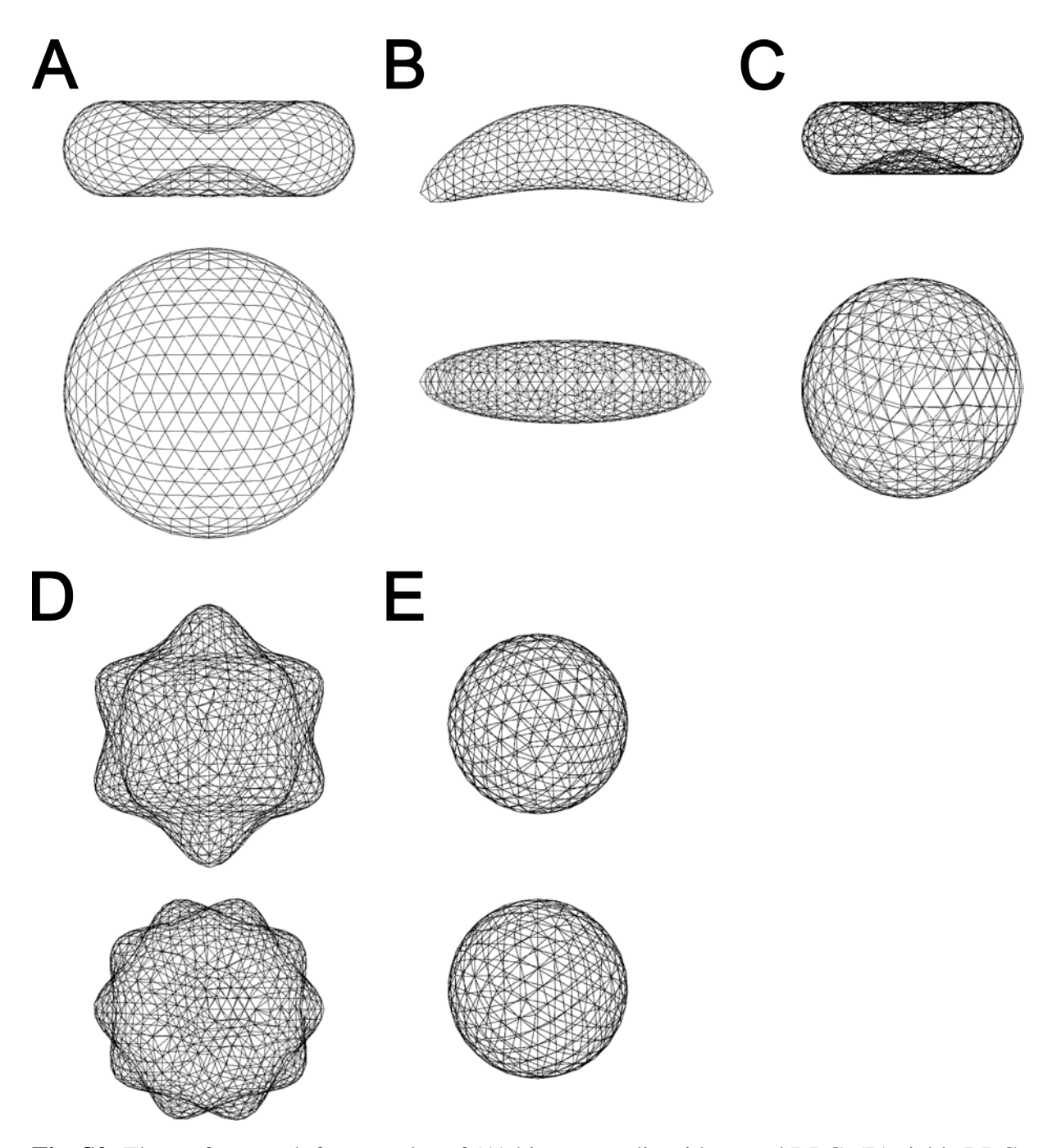


**Fig. S2.** The surface mesh for capsules of (A) biconcave-discoid normal RBC, (B) sickle RBC, (C) iron deficiency RBC, (D) sphere-echinocyte, and (E) spherocyte. Note the size of each cell species in this figure is corresponding to the cell used in our simulation. The radius of normal RBC is  $4\mu m$ ; aberrant RBCs are smaller than normal RBCs.

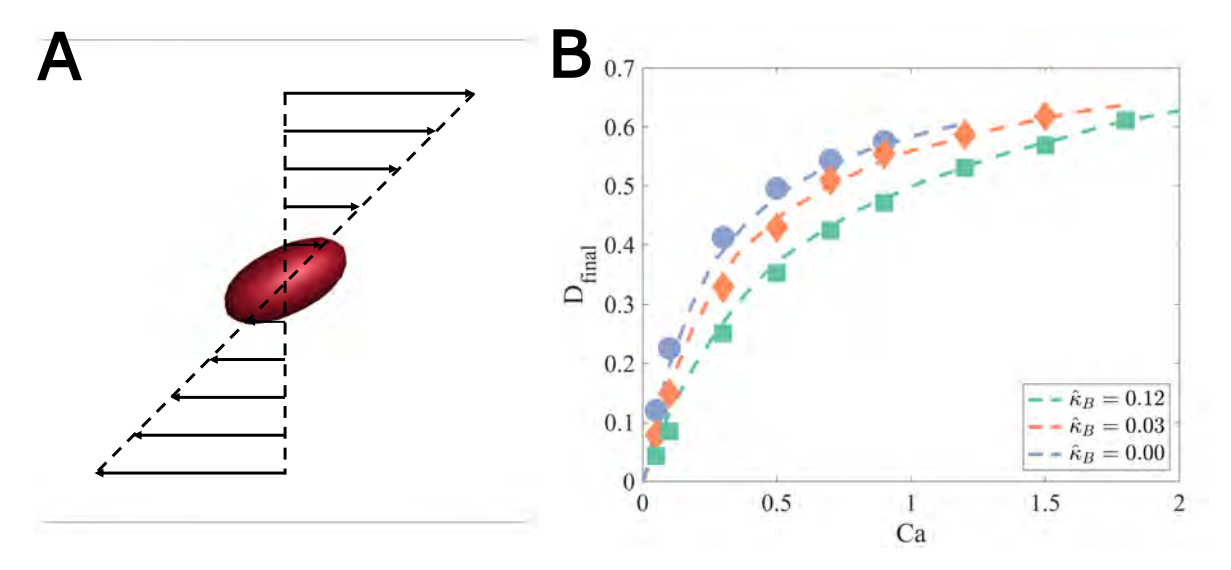


**Fig. S3.** (A) Schematic diagram of an elastic spherical capsule in simple shear flow. Velocity Dirichlet boundary conditions are imposed on both the top and bottom plates to create a simple shear flow. Because of the existence of a constant shear rate, the sphere capsule is stretched and then deformed into an ellipsoid. (B) Steady-state Taylor deformation parameter for a spherical capsule as a function of Ca. Dash lines are results from previous literature (72), and symbols are our simulation results.

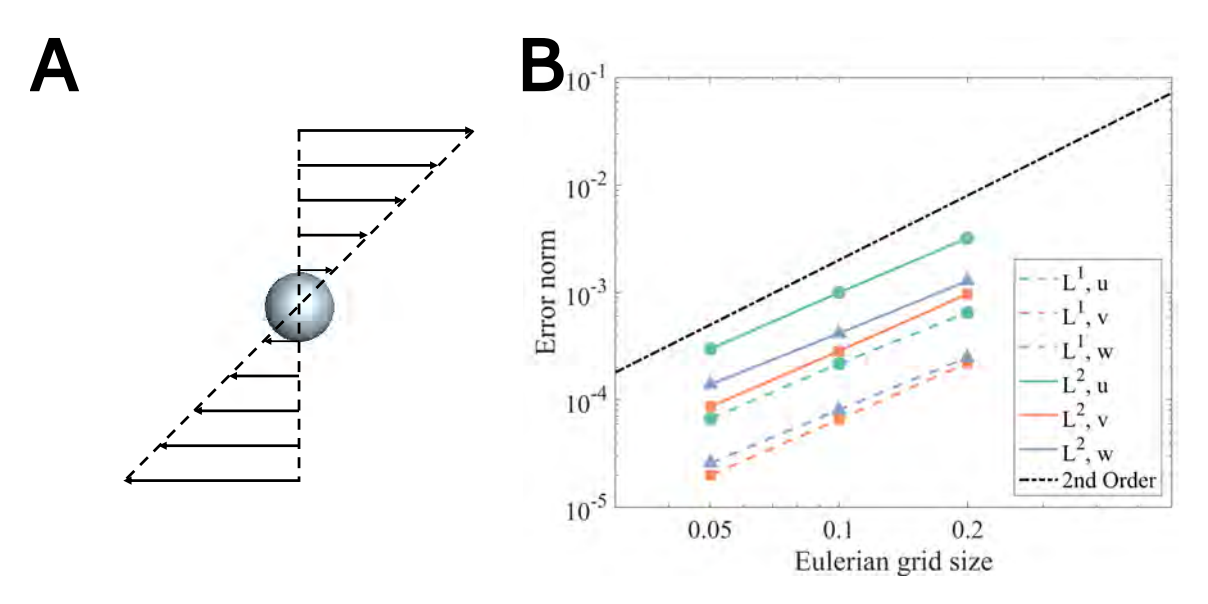


**Fig. S4.** (A) Schematic of simulating a rigid stationary sphere subjected to a linear shear flow. The velocity field on the top and bottom wall is set to be the analytical solution (Dirichlet boundary condition). Periodic boundary conditions are imposed along x and y direction. A rigid sphere is placed at the center of the box. The velocity on the sphere surface is set to zero. (B) Error norm vs. mesh size for stationary rigid sphere in a linear shear flow

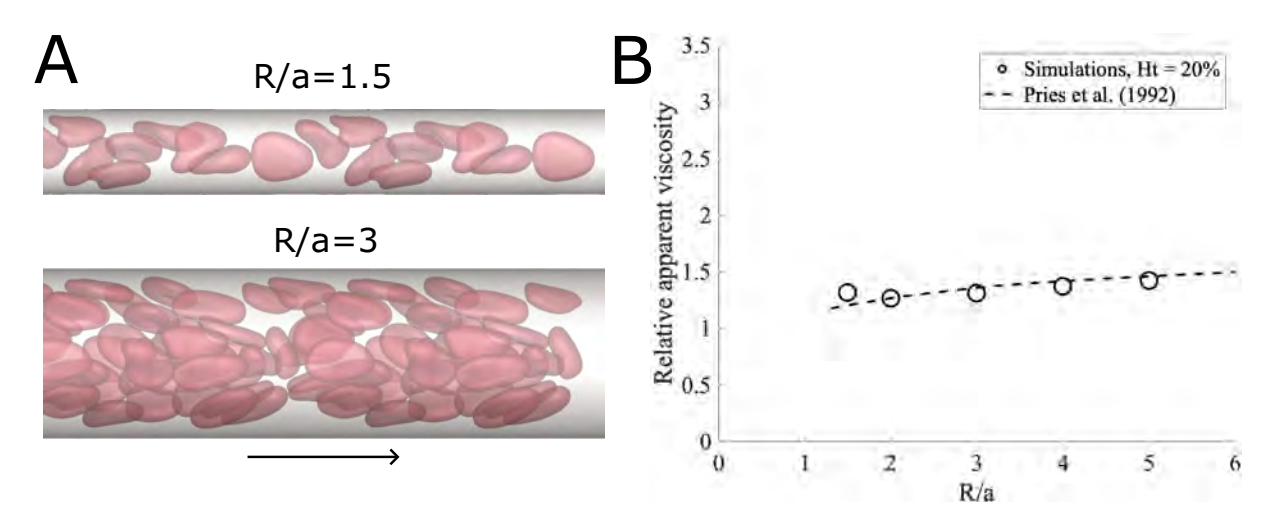


**Fig. S5.** (A) Simulation snapshots of healthy RBCs with radius  $a=4\mu m$  flowing through tubes of various radius R. Hematocrit is set to be 20%. The arrow indicates the direction of flow. (B) The relative apparent viscosity as a function of tube radius R and comparison with experimental relation in (74).

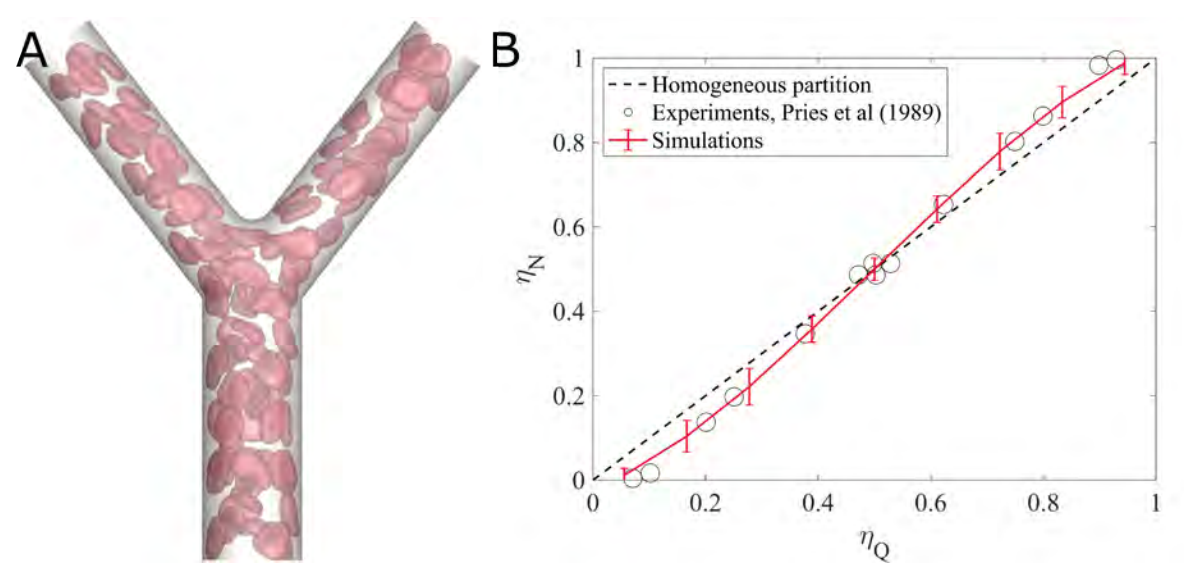


**Fig. S6.** (A) Simulation snapshots of healthy RBCs partitioning near a bifurcation. The radius of the inlet vessel is  $10\mu m$ . (B) Comparison of the Zweifach-Fung effect in our simulation with experimental results from past literature (76).

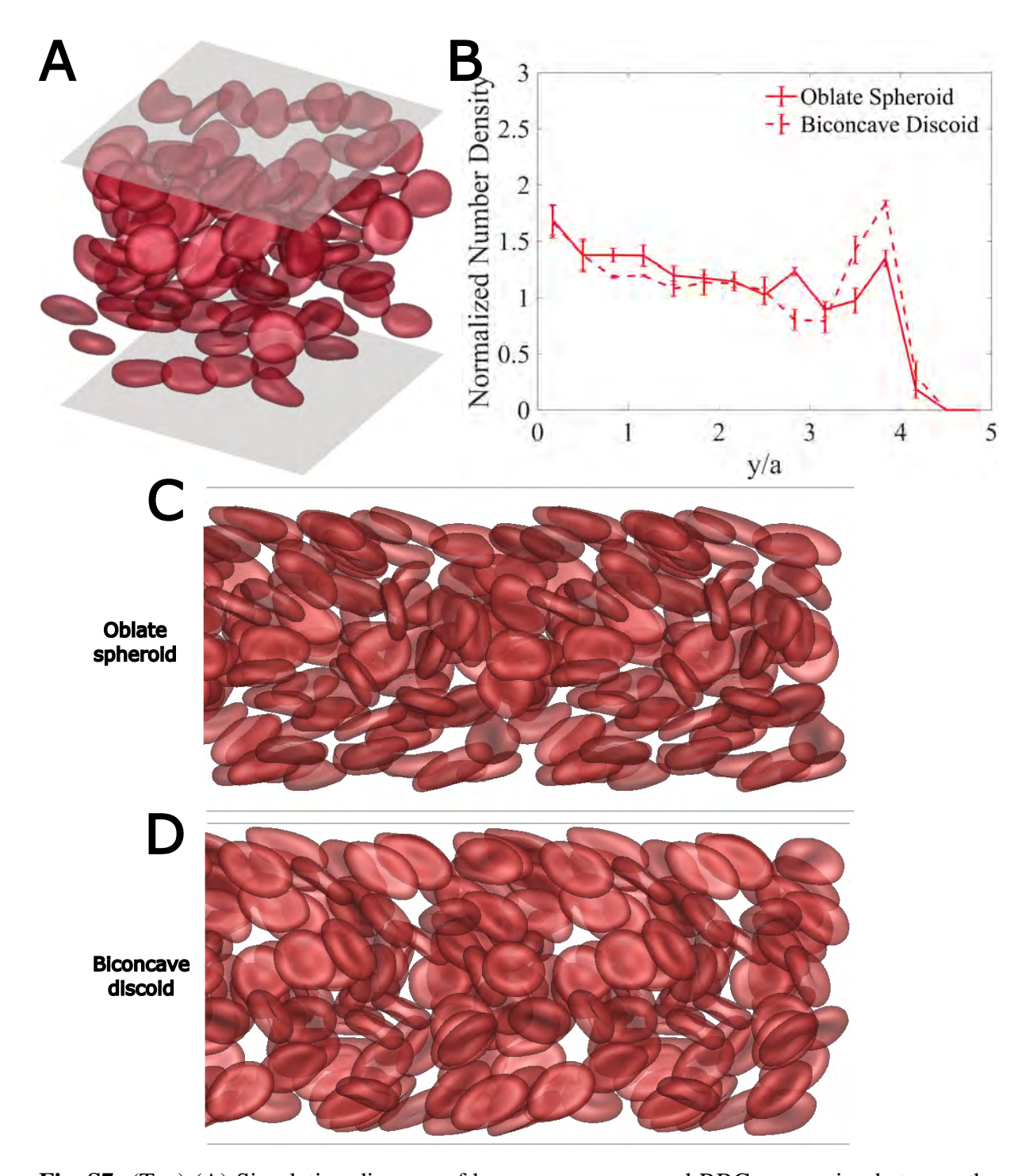


**Fig. S7.** (Top) (A) Simulation diagram of homogeneous normal RBC suspension between the slit under pressure-driven flow. ( $Re_p = 0.1$ , Hematocrit = 0.15)(B) Steady-state wall-normal direction cell number density profile. Note here y/a = 0 denotes the slit center and y/a = 5 close to the wall. (Bottom) The side view of RBC suspension with bending spontaneous curvature being (C) oblate spheroid and (D) biconcave discoid.

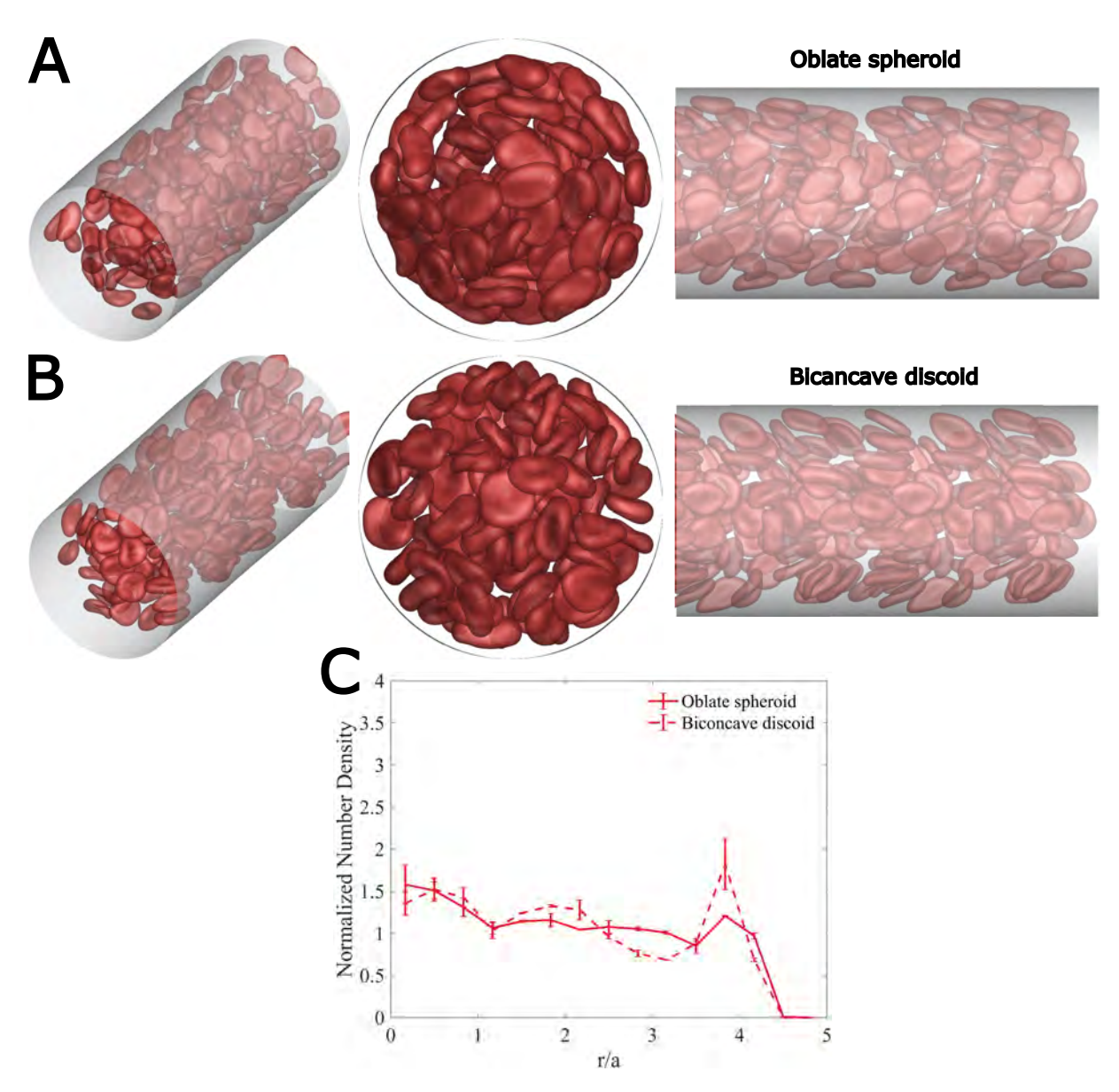


**Fig. S8.** (Top)Simulation snapshots for homogeneous normal RBC suspension within the straight cylindrical tube with spontaneous bending curvature being (A) oblate spheroid and (B) biconcave discoid. ( $Re_p$ =0.1, Hematocrit = 0.20). (Bottom) (C) Steady-state radial cell number density profile for two types of RBC suspensions.

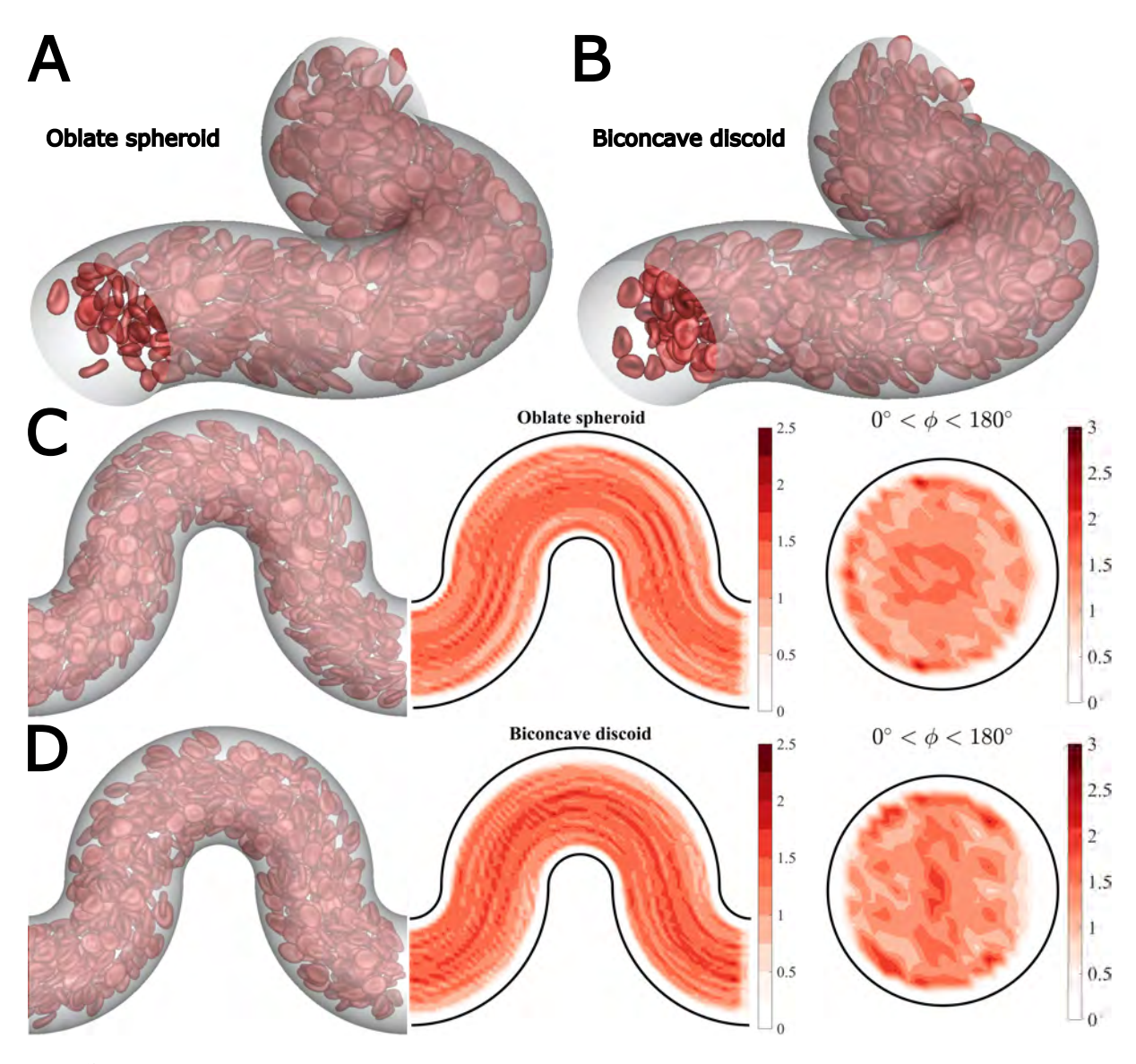


**Fig. S9.** (Top) Simulation snapshots for normal RBC suspension in the curved serpentine channel with spontaneous curvature being (A) oblate spheroid and (B) biconcave discoid. (Bottom) Center-plane and cross-sectional cell number density distribution for RBC suspension with spontaneous curvature being (C) oblate spheroid and (D) biconcave discoid.

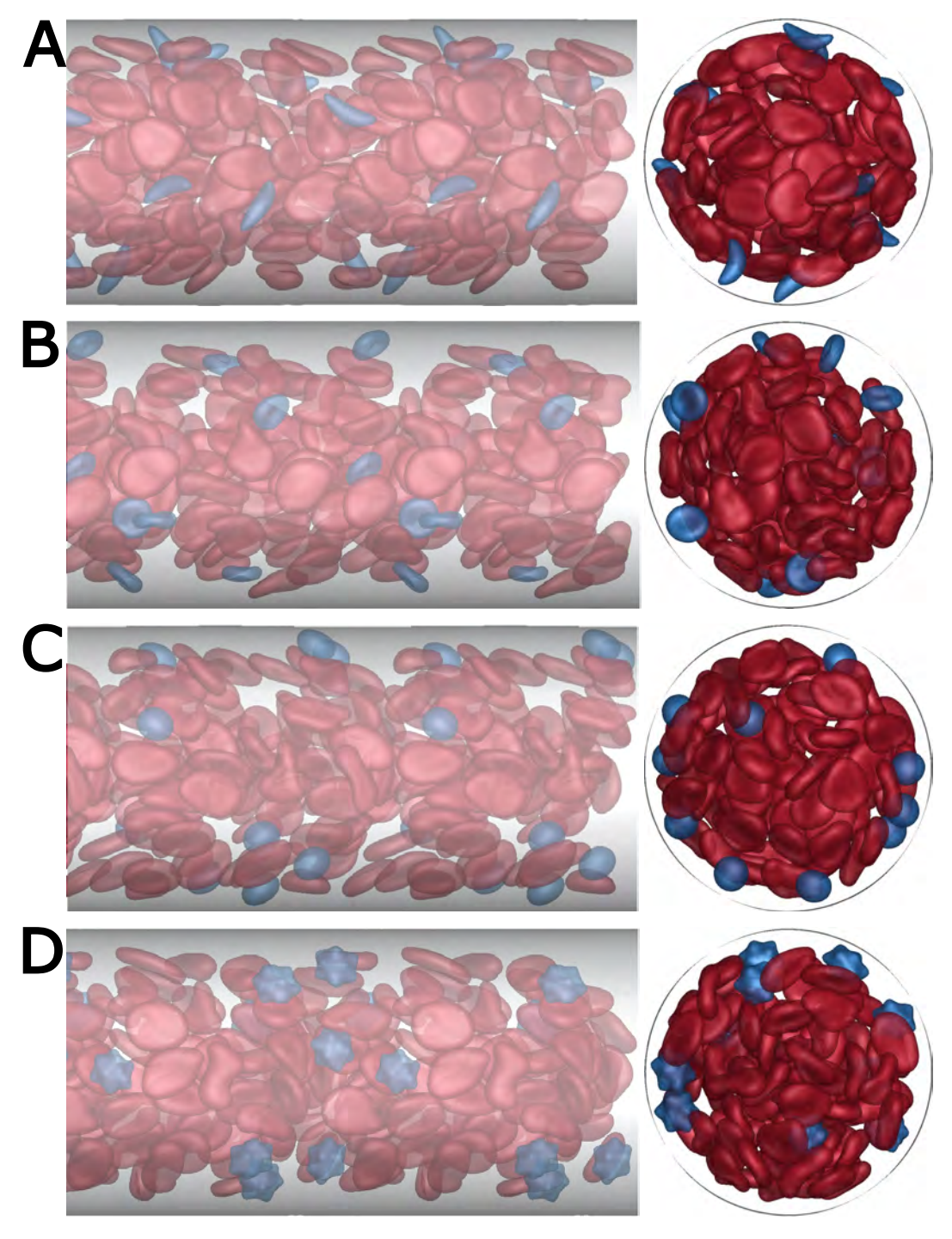


**Fig. S10.** Simulation snapshots (left: side view; right: top view) for (A) SCD, (B) IDA, (C) spherocytosis, and, (D) COVID-19 RBC suspension in the cylindrical straight channel.

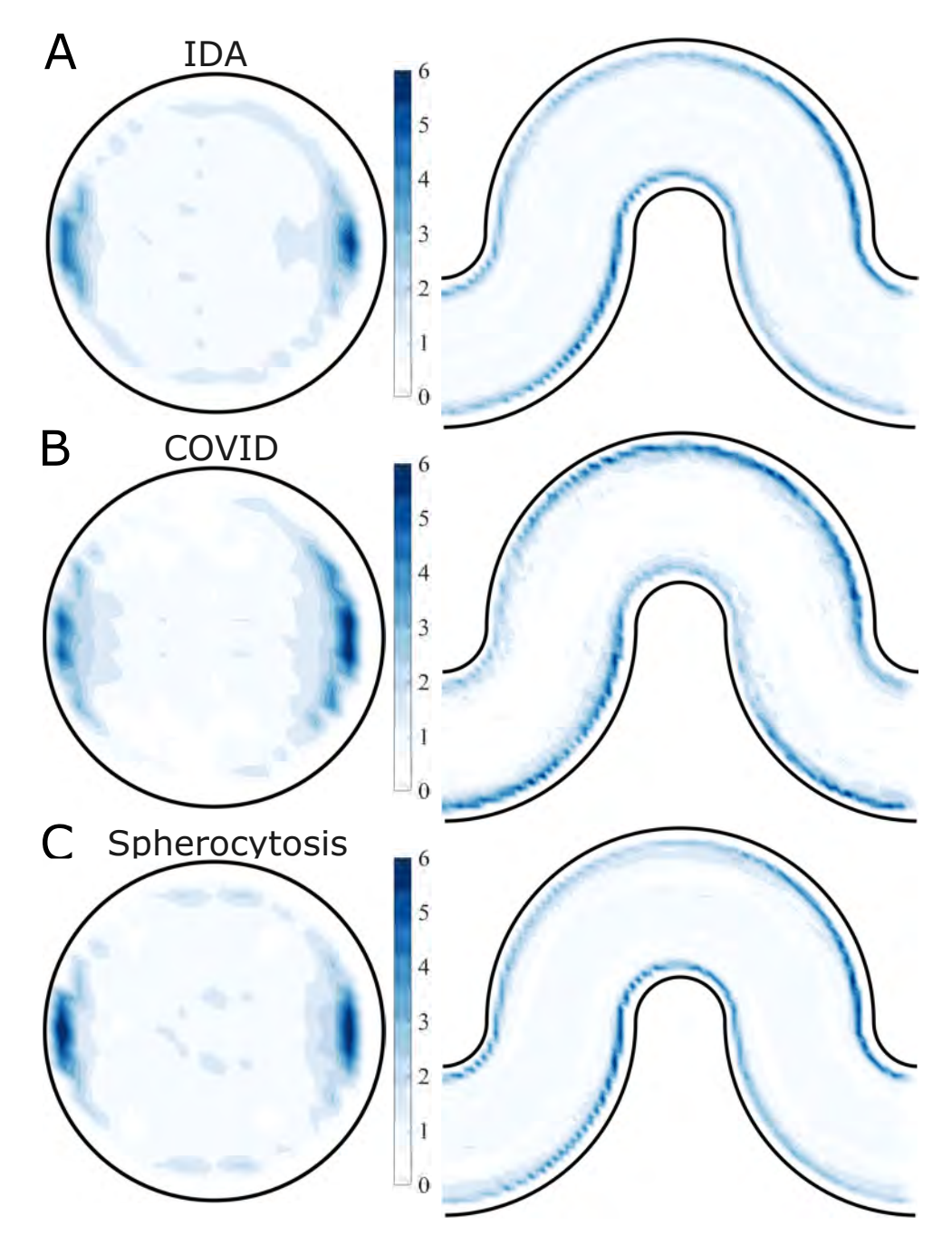


**Fig. S11.** Distributions of aberrant cells within a curved blood vessel. Cross-sectional and center-plane normalized cell number density distribution of (A) iron deficiency RBCs, (B) sphero-echinocytes, and (C) spherocytes over the entire curved channel ( $0^{\circ} < \theta < 180^{\circ}$ ) in each corresponding binary suspensions of normal RBCs with aberrant RBCs.

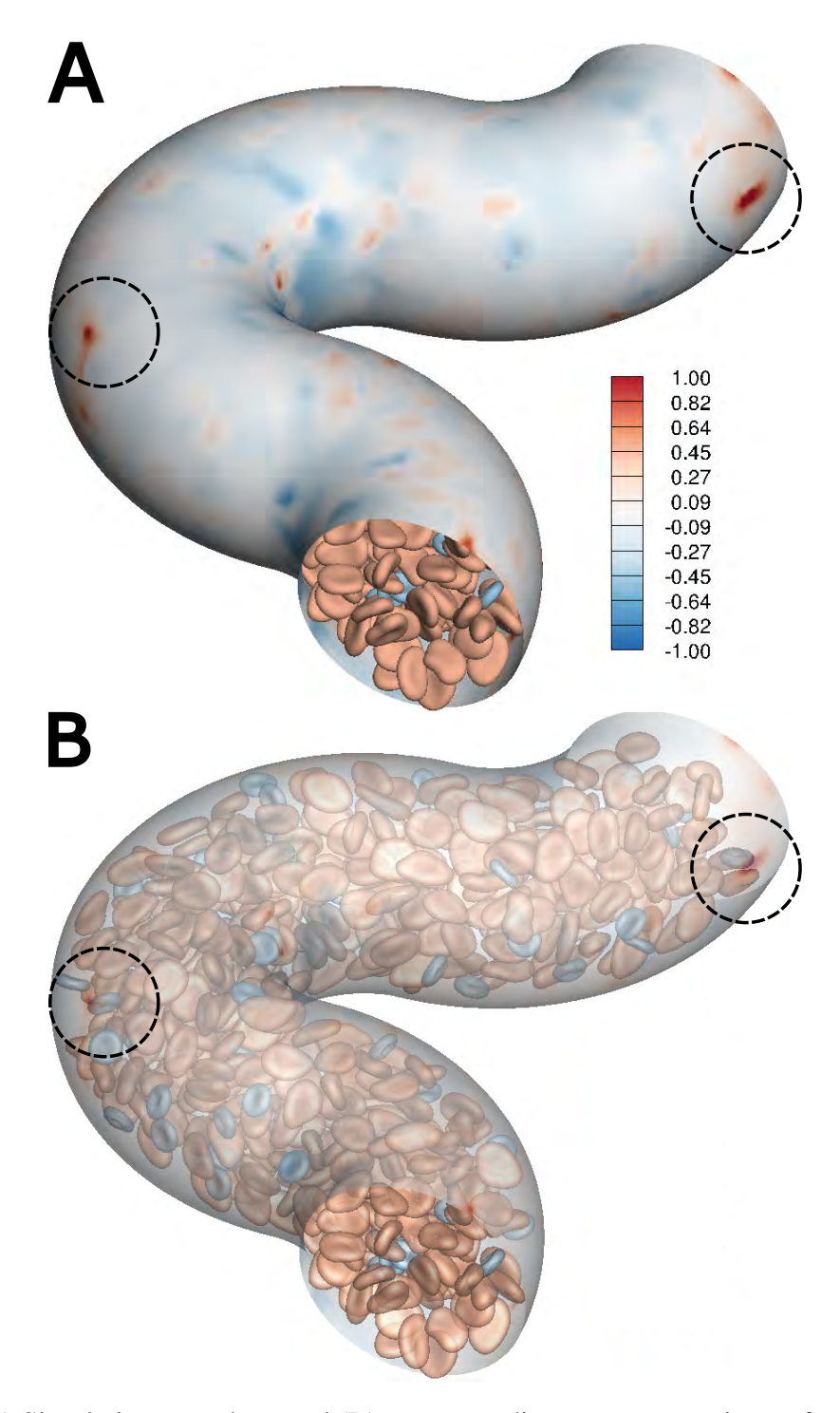


**Fig. S12.** (A) Simulation snapshots and (B) corresponding transparent views of additional wall shear stress  $\hat{\tau}_w$  induced by the presence of the cells in suspensions of normal RBCs with iron deficiency RBCs within the serpentine channel. The color on the serpentine vascular surface denotes the RBC-induced wall shear stress strength  $\hat{\tau}_w$ .

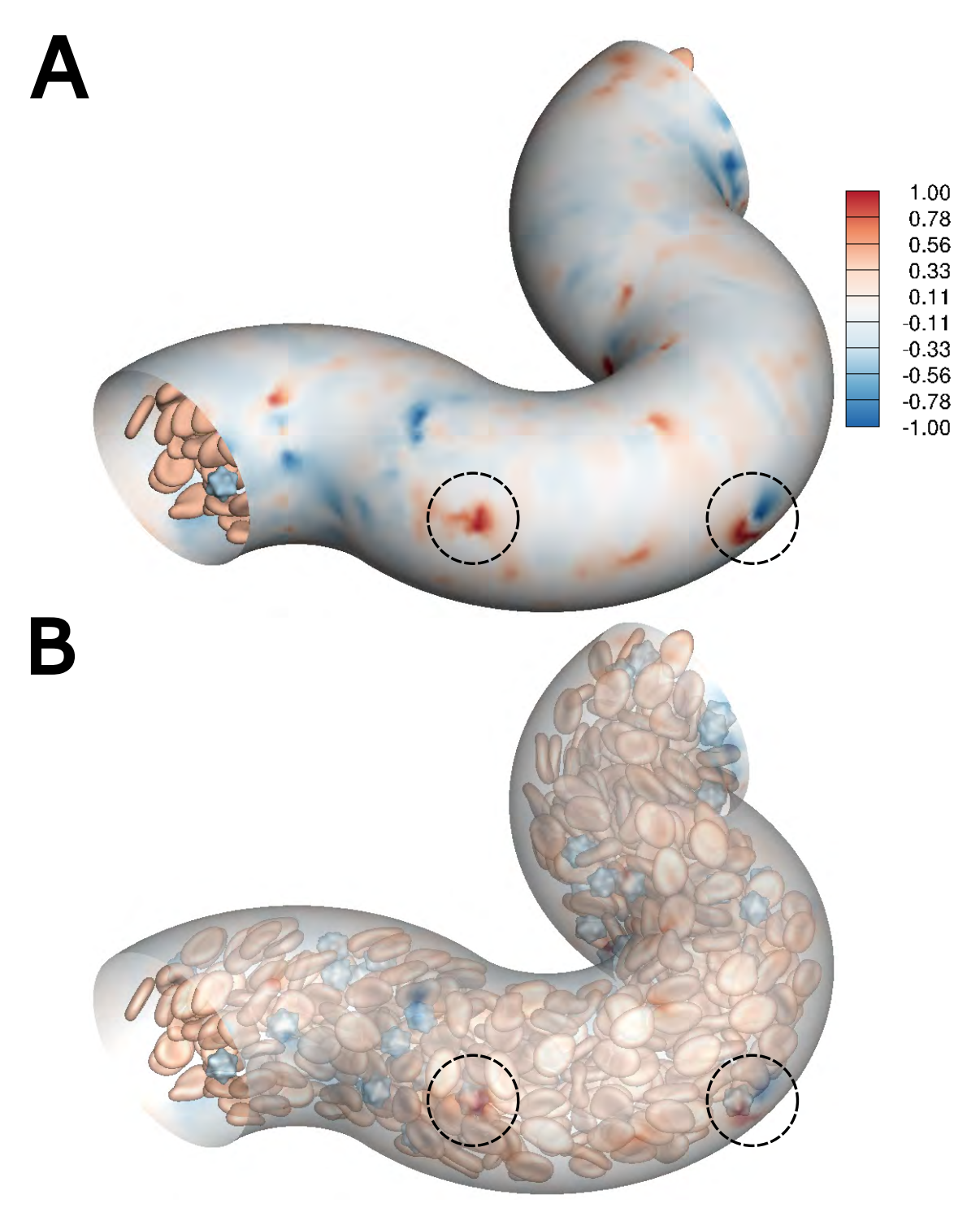


**Fig. S13.** (A) Simulation snapshots and (B) corresponding transparent views of additional wall shear stress  $\hat{\tau}_w$  induced by the presence of the cells in suspensions of normal RBCs with spheroechinocytes within the serpentine channel. The color on the serpentine vascular surface denotes the RBC-induced wall shear stress strength  $\hat{\tau}_w$ .

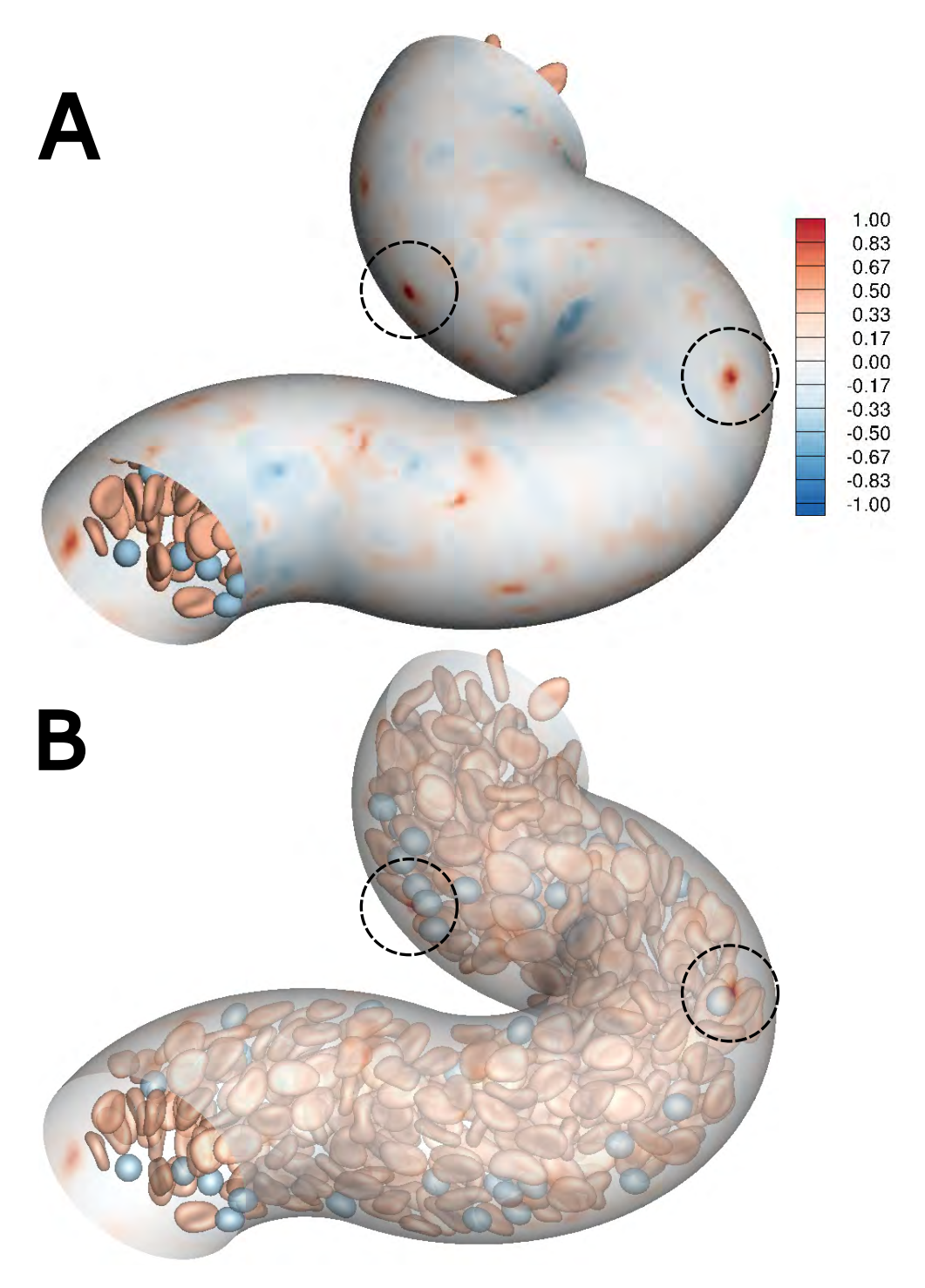


**Fig. S14.** (A) Simulation snapshots and (B) corresponding transparent views of additional wall shear stress  $\hat{\tau}_w$  induced by the presence of the cells in suspensions of normal RBCs with spherocytes within the serpentine channel. The color on the serpentine vascular surface denotes the RBC-induced wall shear stress strength  $\hat{\tau}_w$ .